Research Square

Preprints are preliminary reports that have not undergone peer review. They should not be considered conclusive, used to inform clinical practice, or referenced by the media as validated information.

A Single-Cell Atlas of Liver Metastases of Colorectal Cancer Reveals the Reprogramming of the Tumor Microenvironment in Response to Preoperative Chemotherapy

Jian-Ming Li (lijming3@sysu.edu.cn)
Sun Yat-sen Memorial Hospital, Sun Yat-sen University

Li-Heng Che
Sun Yat-sen Memorial Hospital, Sun Yat-sen University

Jing-Wen Liu
Sun Yat-sen Memorial Hospital, Sun Yat-sen University

Rong Luo
Department of Pathology, Sun Yat-sen Memorial Hospital, Sun Yat-sen University, Guangzhou

Jian-Ping Huo
Sun Yat-sen Memorial Hospital, Sun Yat-sen University

Yu-Qing Li
Sun Yat-sen Memorial Hospital, Sun Yat-sen University

Ai-Jun Zhou
Sun Yat-sen Memorial Hospital, Sun Yat-sen University

Piao Huang
Sun Yat-sen Memorial Hospital, Sun Yat-sen University

Yong-Yu Chen
Sun Yat-sen Memorial Hospital, Sun Yat-sen University

Wen Ni
Sun Yat-sen Memorial Hospital, Sun Yat-sen University

Yunxia Zhou
Xiamen University

Yuan-Yuan Liu
Sun Yat-sen Memorial Hospital, Sun Yat-sen University

Hui-Yan Li
Sun Yat-sen Memorial Hospital, Sun Yat-sen University

Rong Zhou
Sun Yat-sen Memorial Hospital, Sun Yat-sen University

Hui Mo
Shandong University School of Medicine

Article

Keywords: Single-cell RNA sequencing, Preoperative chemotherapy, Liver Metastases of Colorectal cancer, Tumor microenvironment

Posted Date: October 9th, 2020

DOI: https://doi.org/10.21203/rs.3.rs-84915/v1

License: This work is licensed under a Creative Commons Attribution 4.0 International License.
Read Full License

Abstract

Metastasis is the primary cause of cancer-related mortality in colorectal cancer (CRC) patients. How to improve therapeutic options for patients with metastatic CRC (mCRC) is the core question for CRC treatment. However, the complexity and diversity of stromal context of the tumor microenvironment (TME) in liver metastases of CRC is not fully understood, and its influence on response to chemotherapy is unclear. Here we provide an in-depth analysis of transcriptional landscape of primary CRC, matched liver metastases and blood at single-cell resolution, and perform a systematic examination of transcriptional changes and phenotypic alteration of the TME in response to preoperative chemotherapy (PC). Based on 111,292 single-cell transcriptomes, our study reveal that TME of treatment-naïve tumors is characterized by higher abundance of less-activated B cells and higher heterogeneity of tumor-associated macrophages (TAMs). By contrast, in tumors treated with preoperative chemotherapy, we find reprogramming of B cell activation, lower diversity of TAMs with immature and less activated phenotype, lower abundance of both dysfunctional T cells and ECM-remodeling cancer-associated fibroblasts (CAFs), an accumulation of myofibroblast. Our study may provide a foundation to investigate the cellular mechanisms underlying liver metastasis of CRC and response to preoperative chemotherapy, and open up new possibilities for predicting and guiding therapeutic responsiveness.

Introduction

Metastasis is the primary cause of cancer-related mortality in colorectal cancer (CRC) patients (Jemal et al., 2011; Vatandoust, 2015). The 5-year survival rate of CRC patients at the advanced stage (stage IV) is only about 12% (Miller et al., 2019). In CRC, liver is the most frequent site of metastases. For the patients of metastases of colorectal cancer (mCRC), surgical resection of both primary and metastases is the best option for curative treatment (Adam et al., 2004; Brandi, 2016; Cameron, 2017; Van Cutsem et al., 2010; Hackl et al., 2014). However, mainly for the size, number and location of liver metastases, only a minority of patients is suitable for upfront surgery (~ 20%) (Lise et al., 2003; Siegel et al., 2012). Moreover, even after resection, due to the latent disseminated tumor cells after surgery, relapse is very common (occurs in 75% of patients) (Jemal et al., 2011; Nordlinger et al., 1996; Tauriello et al., 2017). Thus, surgery in combination with chemotherapy and/or immunotherapy become an accepted standard of care for CRC patients with liver metastases.

Preoperative chemotherapy (PC) aims at reducing tumor load, which may reduce the risk of local relapse and promoting patients with initially unresectable mCRC to resectable liver metastases (Glimelius et al., 2013; Kapiteijn et al., 2001). Nevertheless, despite theoretical benefit and randomized trail demonstrations (Nordlinger et al., 2008), whether the patients undergoing chemotherapy and resection have long-term benefit is still questionable. How to provide optimal treatment of CRC patients with liver metastasis remains a pivotal issue.

Understanding the complex cellular and phenotypic diversity within the tumor microenvironment (TME) may pave the way for the development of effective treatment in cancer especially in metastatic disease.

Recently, single-cell RNA sequencing (sc-RNA) greatly contribute to our understanding of TME in many cancers, including melanoma (Davidson et al., 2018; Li et al., 2019; Tirosh et al., 2016), head and neck cancer (Puram et al., 2017), hepatocellular carcinoma (Zhang et al., 2019a; Zheng et al., 2017), lung carcinoma (Guo et al., 2018; Lambrechts et al., 2018; Lavin et al., 2017), breast carcinomas (Azizi et al., 2018; Savas et al., 2018; Wagner et al., 2019; Chung et al., 2017), kidney cancer (Chevrier et al., 2017) and basal cell carcinoma (Yost et al., 2019). In colorectal cancer, single-cell genomic (Leung et al., 2017; Roerink et al., 2018), transcriptome (Bian et al., 2018; Li et al., 2017; Zhang et al., 2018, 2019b) and epigenomic analyses (Bian et al., 2018) provided new insights into intra-tumor genomic diversity and inter-tumor difference. Despite recent advances in our understanding of CRC, the cellular milieu of liver metastases and their primary counterparts are still poorly understood. How TME response to chemotherapy in primary tumor and their corresponding liver metastases are largely unexplored.

In this study, we established a landscape of TME of liver metastases of CRC based on 111,292 single cells, and uncovered the transcriptional changes and phenotypic alteration of TME in response to chemotherapy. We found that preoperative chemotherapy may promote the activation of B cells, drive down the diversity of TAMs, recruit more immature TAMs, MHC ^{low} TAMs and myofibroblast, decrease the abundance of dysfunctional T cells and ECM-remodeling CAFs. We also find the key ligand-receptor based cellular interactions in the cellular milieu of tumors treated with PC and treatment-naïve tumors, in both primary and the metastases of CRC. Taken together, we established a single cell atlas of TME in both primary CRC and matched liver metastases with or without chemotherapy at single-cell resolution. This resource provided a foundation to investigate the cellular mechanisms in liver metastasis and therapeutic response, and facilitate the development of novel treatment to mCRC.

Results

1. single-cell analysis of tumor microenvironment of liver metastases of colorectal cancer.

To gain a better understanding of tumor microenvironment, and investigate how TME response to preoperative chemotherapy in liver metastases of CRC, we performed scRNA-seq of 15 samples from three sites (primary CRC, matched liver metastases and blood) of six CRC patients with liver metastatic disease (Table S1). While patients COL15, COL17 and COL18 have been treated with preoperative chemotherapy, the others are treatment naïve. All patients were classified as microsatellite-stable (MSS) with invasive adenocarcinomas and late-stage (IV) disease (Methods, Table S1).

Viable single cells were sorted and used for droplet-based single-cell RNA sequencing (scRNA-seq). After quality control (see Methods), we obtained transcriptome data for 111,292 single cells from primary CRC (n = 6), matched liver metastases (n = 6), and PBMCs (n = 3) for liver metastases of CRC (Table S2). Then we clustered single cells using shared nearest neighbor (SNN) clustering based on significant principal components (PCs), and visualized cell clusters using t-distributed stochastic neighbor embedding (*t*-SNE) (Fig. 1a, Methods). The major cell populations (including T cells /natural killer (NK) cells, B/plasma cells,

cancer-associated fibroblasts (CAFs), endothelial and myeloid cells) were annotated with canonical marker genes (Fig. 1b), treatment state and tissue origin are mapped in Fig. 1c (also see Figure S1a), selected representative markers of each cell type is presented in Fig. 1d and Fig. 1e and Figure S1b.

To characterize the ecosystems of primary and metastatic tumor in CRC, and better understand how TME response to preoperative chemotherapy in liver metastases of CRC, we focus on major cell types of TME (T/ NK cells, B cells, Myeloid cells and CAFs), for each compartment, we re-centred, scaled, normalized and re-clustered the data. Ultimately, we obtained 28 myeloid clusters (6 dendritic cells, 18 tumor-associated macrophages (TAMs), 1 monocytes, 2 myeloid-derived suppressor-like cells (MDSCs-like) and 1 mast cells), 17 B cell clusters, 10 mesenchymal cell clusters (1 endothelial, 6 cancer-associated fibroblasts and 3 myofibroblasts) and T/NK cell clusters. Each cluster was composed of cells from different patients, and for each cluster, the distribution of tissue and treatment status were different (Figure S1c).

2. Preoperative chemotherapy promotes the activation of B cells in the primary CRC

First, we investigate how preoperative chemotherapy influenced the ability of B cells. Interestingly, B cells were prevalent in primary CRC (account for 0.1% of all stromal cells in primary CRC), but depleted significantly in liver metastases (account for 0.01% of all stromal cells in liver metastases) (Fig. 2a). Sub-clustering of B cells revealed 17 subpopulations (Fig. 2b). Among them, 15 clusters were mature B cells (with eight subsets from tumor lesion and five clusters from peripheral blood, Fig. 2b), which are characterized by highly expression of CD20 (MS4A1). While cluster 3 represents plasma cells which is characterized by highly abundant immunoglobulin (IGHG1, IGHG2, IGHG3, IGHG4 and IGHA2), cluster 16 represent plasmablast, characterized by upregulation of immunoglobulin and cell proliferation markers (e.g. MKI67, CDC20, CDKN3 and CCNB2) (Table S3).

Since few B cells infiltrated in the liver metastases, we mainly focused on B cells in the primary CRC. In primary tumor, B cells were separated into different compartments, the B cell populations from tumor treated with preoperative chemotherapy were quite distinct from that in treatment-naïve tumors (Fig. 2c and 2d). We found that cluster 0, 2, 6 and 11 were enriched specific in treatment-naïve tumors, whereas cluster 1, 4, 9, 10 and 12 were almost exclusively present in treated tumors (Fig. 2c, 2d).

On closer examination of the two groups, we find that they had distinct phenotypes (Table S3). Untreated tumors-derived B cells exhibited a naïve and inflammatory phenotype, with cluster 6 expressing IgD (*IGHD*), cluster 0 expressing immature B cell marker VPREB3 and cluster 2 expressing inflammatory transcription factor NF-kB (NFKBIA), lipid molecules (e.g. APOE and APOC1) and cytokines (e.g. AREG).Whereas B cells derived from treated tumors (cluster 1, 4, 9, 8 and 12) have an activated immune

activation phenotype with upregulation of immunocostimulatory molecules (e.g.,CD82, CD83 and CLECL) and MHCs molecules (e.g.,HLA-DRA, HLA-DRB5) (Table S3). GO analysis also confirms that upregulated genes associated with treated tumors were enriched in antigen processing and presentation (Figure S2a).

Comparing with B cells in untreated tumors, higher expression of immunoglobulin, such as IGLC3, JCHAIN, IGHG1, IGHG3, IGHG4 and IGHA1, were observed in treated tumors (Fig. 2e, 2f, and Figure S2b), implying class switch recombination (CSR, also known as isotype switching) may occur after preoperative chemotherapy. Moreover, the expression of MHCs molecules (such as HLA-A, HLA-DQB1, HLA-DQA2 and HLA-DRB1) were also elevated in treated tumors (Fig. 2g). In line with these results, GO analysis shows that B cells in tumors treated with PC enriched in immune activation signaling pathway, including immune response-activating cell surface receptor, antigen processing and presentation signal pathway, and T cell co-stimulation (Fig. 2h). Whereas B cells in treatment-naïve tumors were enriched in process of responding to reactive oxygen species (ROS), a general feature of inflammation. Thus, those results support the phenotype of B cells in treatment-naïve tumors are associated with inflammation. On the contrary, in tumors treated with preoperative chemotherapy, preoperative chemotherapy promote the activation and the generation of class-switched antibody of B cells.

If B cells can contribute to anti-tumor processes, an effective immune response against tumor progress may be reflected by the presence of a gene expression signature of B cell activation. This lead us to hypothesize that gene expression signatures of activated B cells may be correlated with prognosis of colorectal cancer. To test this, we turn to The Cancer Genome Atlas (TCGA) colon adenocarcinoma (COAD) clinical data, and found the gene signatures of activated B cells were associated with a good prognosis in CRC patients marginally significantly (Fig. 2i, n = 266, including MSI-high, MSI-low and MSS subtype, p = 0.05, Cox regression). Interestingly, the correlation become more prominent in MSS tumors (Fig. 2j, n = 174, MSS subtype, p = 0.034, Cox regression), suggesting that activation of B cells could be more effective in MSS tumors.

Collectively, our data demonstrate that preoperative chemotherapy promotes B cells from a less activated and inflammatory state to a switched and more activated state in the primary tumor of CRC patients with liver metastases, and the activation of B cell could be a potential predictor of effective chemotherapy and good prognosis, especially in patients with MSS CRC. This was also reported in tumors treated with immunotherapy in recently studies (Cabrita et al., 2020; Helmink et al., 2020; Hollern et al., 2019; Petitprez et al., 2020).

3. Preoperative chemotherapy reprogramming TAMs from highly heterogeneity to immature and less activated phenotypes

Myeloid cells are the key components in tumor microenvironment, with an important role in tumor progression and metastasis (Qian et al., 2010).We identified 15,366 myeloid cells, sub-clustered into 28 clusters. Among these myeloid compartments, we designated 18 clusters of tumor-associated

macrophages (TAMs), which displayed various features. One cluster of monocytes (M25: *FCGR3A*) and two clusters of myeloid-derived suppressor-like cells (MDSCs-like, M02 and M16). Six clusters were DCs, including CD1c + DCs (M07 and M10: *CD1C*), cross-presenting DCs (M21: *CLEC9A*), pDCs (M17 and M27: *LILRA4*) and LAMP3 + DCs (M22: *LAMP3*) (Zhang et al., 2019a). One cluster represents mast cells (M05: *TPSAB1*). The selected marker genes in myeloid cells were presented in Figure S3a. While TAMs and DCs were enriched in both primary tumor and liver metastases, monocytes and MDSCs-like cells were prevalent in blood and mast cells were mainly enriched in primary CRC (Fig. 3a and 3b).

M02 and M16 enriched the signature of myeloid-derived suppressor cells (MDSCs) (Condamine et al., 2016; Zhao et al., 2012). Consistent with results in Zhang et al., 2019a, S100A family genes are highly expressed, including S100A12, S100A9, S100A8, together with FCN1 and VCAN, but MHC I and MHC II molecules tend to be lowly expressed (Table S3).

Macrophages commonly function as phagocytic cells, which can be activated and display varying phenotype in response to different stimulations (Buckley, 2019; Ngambenjawong et al., 2017). For the diversity and plasticity of TAMs, their heterogeneity and impacts on tumor progression remains largely uncharacterized (Engblom et al., 2016). In this study, we identified a total of 18 clusters of tumor-associated macrophages (TAMs), with no clear delineation between the phenotypes between M1 and M2, the M1 and M2 gene signatures are positively correlated in our TAMs compartment (Figure S3b), indicating that TAMs were more complex than the classical M1/M2 model, consistent with previous studies (Azizi et al., 2018; Cassetta et al., 2019; Davidson et al., 2018; Müller et al., 2017; Zhang et al., 2019a; Zheng et al., 2011). Based on the transcription state and expressed genes of TAMs, we identified various signature genes and classed 18 clusters TAM into four major TAM subsets (Fig. 3c).

The first subset, including cluster 0, 12 and 13, were classified as MHC ^{low} TAMs. MHC ^{low} TAMs exhibited weak capacity of antigen presentation and immune activation, with lowly expressed MHC I and MHC II genes (e.g. HLA-A, HLA-C, HLA-DRA and HLA-DRB1), and lowly expressed immune-costimulatory genes (e.g. CD80 and CD86). Cluster 12, classified as IL1B + MHC ^{low} TAMs, characterized by upregulation of a large number of inflammatory and chemokine genes (e.g., IL1B, IL6, S100A9, S100A8, CXCL8, CXCL3 and CXCL1) which involved in recruiting and regulating of immune cells. Cluster 12 were presented in the primary CRC, in patients who are treatment-naïve (Fig. 3c, right panel, Fig. 3d). Cluster 0 (THBS1 + MHC ^{low} TAMs) were prevalent in liver (Fig. 3c, right panel), with highly expression of THBS1, MARCO and genes promoting proliferation of epithelia cells and angiogenesis, such as EREG, AREG and VEGFA, which could stimulate tumor growth and progression. Cluster 13 (MARCO + MHC ^{low} TAMs), mainly derived from liver resident Kupffer cells (KCs; the tissue resident macrophage of liver), may exert a tolerogenic or immune inhibitory functions in the liver metastases through MARCO, VSIG4 and CD163.

The second subset, including cluster 6, 9, 14, 18 and 19, were classified as lipid-associated TAMs (LAMs), which were characterized by upregulation of genes involved in lipid metabolism (e.g., APOC1, APOE and LPL), extracellular matrix (ECM) degradation (e.g., MMP7, MMP9 and SPRAC) and complement activation (e.g., C1QA, C1QB and C2). They also highly expressed TREM2 (encoding lipid receptor) and

LGALS3 (associated with immune suppression), which were recently found to be associated with metabolic diseases (Jaitin et al., 2019). Among the subset, cluster 6 and cluster 9 showed higher expression levels of matrix metalloproteinases (MMPs) compared to other clusters. GO analysis of upregulated genes in each cluster demonstrated that TAMs were enriched in neutrophil activation and degranulation (Figure S3c). In the primary CRC, lipid-associated TAMs (LAMs) is mainly presented in treatment-naïve tumors, but is shared in treated and untreated in the liver metastases (Fig. 3c, right panel, Fig. 3d).

The third subset, including cluster 4 and 11, were enriched for genes involved in regulation of myeloid leukocyte differentiation, were prevalent in tumors treated with PC (Fig. 3c, right panel, Fig. 3d). With highly expression of FOS, cluster 4, mainly from liver metastases, may be monocyte-derived, which could differentiate into macrophage (Azizi et al., 2018). In addition to the canonical myeloid marker gene CD33, cluster 11 was also associated with highly expression of CD4, which is typically expressed by monocytes and involved in triggering cytokine expression and the differentiation of monocytes into functional mature macrophages (Azizi et al., 2018; Dumitru et al., 2012; Zhen et al., 2014). Moreover, MHC genes tend to be expressed at a higher level in cluster 11 cells than cluster 4, suggesting cluster 11 cells are more mature and activated than the latter. Thus, we classify this subset as monocyte-derived immature TAMs.

The fourth subset, including cluster 20 and 23, are immune regulatory TAMs characterized by upregulation of immune suppressive genes, such as CD274, CCL2, IL10 and TGFB2, and prevalent in primary CRC in treatment-naïve tumors (Fig. 3c, right panel). Strkingly, both of the two clusters are also associated with highly expression of MHC and co-stimulating genes, a signature of immune activation and anti-tumor activities. Together, we uncovered “double-agent” immune regulatory TAMs with co-expression of both immune activated and immune suppressive genes, which indicate complex interactions between anti-tumor and pro-tumor activities.

In addition to the four clusters described above, there are three more clusters, named as M01, M03 and M26, that can not be classified into the above-mentioned five subsets. Genes highly expressed in these three clusters are associated with different bioligical processes and cellular functions. M26 (MKI67 + TAMs) is marked with highly expression of genes in cell proliferation (e.g. MKI67, Table S3). In addition to EGF and MACRO, heat-shock genes are also highly expressed in M01. M03 (CXCL10 + TAMs) highly expressed genes involved in response to interferon-gamma (GBP1, STAT1, IFITM3 and PARP14) and cellular response to zinc ion (MT2A, MT1X and MT1F).

Preoperative chemotherapy reprogramming TAMs from highly heterogeneity to immature and less activated phenotypes

TAMs from treatment-naïve tumors and chemotherapy-treated tumors exhibited distinct phenotypes in both primary tumor and liver metastases. In the primary CRC, TAMs in untreated tumors showed higher heterogeneity, they present distinct phenotypes compared with TAMs in tumors treated with preoperative chemotherapy (Fig. 3d). Focusing on the treatment state, we observed some phenotypes shared between treated and untreated tumors, such as MKI67 + TAMs (M26). However, immature TAMs (M04, M11) and MHC ^{low} TAMs (M00, THBS1 + MHC ^{low} TAMs) were largely specific to treated tumors (Fig. 3e). Instead, clusters of more activated TAMs (MHC ^{high} TAMs, M20 and M23), MMPs + lipid-associated TAMs (M06 and M09), pro-inflammatory TAMs (IL1B + MHC ^{low} TAMs, M12), immune suppressive TAMs (CXCL10 + TAMs, M03) and HSPH1 + TAMs (M01) were specific to treatment-naïve tumors (Fig. 3d, and Fig. 3c, right panel).

Concordant with observations in primary tumors, TAMs populations with heterogeneous phenotypes were presented in both treated and untreated tumors in liver metastasis, including lipid-associated TAMs (M06, M09, M14, M18 and M19) and MKI67 + TAMs (M26). But the MHC ^{low} TAMs (M00, M13) and immature TAMs populations (M04, M11) were dominantly enriched in tumors treated with preoperative chemotherapy (Fig. 3d, 3e). While immune suppressive TAMs (M03, CXCL10 + TAMs) and HSP + TAMs (M01) were enriched in treatment-naïve tumors (Fig. 3d). Importantly, we found the gene signature of M11 is associated with good prognosis marginally significantly ($p = 0.088$, Cox regression, Fig. 3f) in TCGA (The Cancer Genome Atlas) COAD (colon adenocarcinoma) patients with MSS subset ($n = 174$, MSS subtype), but they are not associated with outcomes in MSI CRC tumors, suggesting the infiltration of M11 could be a potential predictor of good prognosis in MSS CRC.

TAMs from tumors treated with PC are distinct from those in treatment-naïve tumors (Figure S3d) at the transcriptome level. In the niche of treatment-naïve tumors, TAMs from the primary CRC were enriched for processes of neutrophil activation, responding to IFN-γ and regulation of fibroblast proliferation (Figure S3d), indicating its proinflammatory phenotype (Lee et al., 2017). TAMs from the metastases enriched for antigen processing and presentation, neutrophil activation and responding to IFN-γ. In the ecosystem of treated tumors, TAMs were characterized by unregulated genes involved in protein targeting to endoplasmic reticulum (ER) and RNA catabolic progress in the primary tumors, while in the metastatic sites, TAMs were enriched for myeloid leukocyte chemotaxis and migration processes, which could be related to monocyte-like TAMs aggregated in this lesion.

In general, our results showed that preoperative chemotherapy suppressed the diversity of TAMs, and only the immature TAMs and THBS1 + MHC ^{low} TAMs infiltrated in the primary tumors, while more TAMs aggregated in liver metastases and tended to be immature and less activated. Thus, chemotherapy reprogramming TAMs from highly heterogeneity to immature and less activated phenotypes

4. Preoperative chemotherapy decreases the abundance of ECM-remodeling CAFs and dysfunctional T cells, but

promotes the accumulation of myofibroblast

In our study, 1383 CAFs were detected and classified into 9 clusters. Notably, CAFs were significantly more abundant in primary CRC than liver metastatic tumor (Fig. 4a). Using gene expression profile, we classified CAFs into three major subsets (Fig. 4b, c), including secretory CAFs (cluster 0, 1, 6 and 7), ECM-remodeling CAFs (cluster 2 and 8) and contractile CAFs (cluster 3, 4 and 5) (Fig. 4b). The subset of secretory CAFs highly expressed secretory genes such as various growth factor (e.g. IGF1, PDGFD, FGF7 and VEGFB) which mediate angiogenesis and cancer cell proliferation, some signal molecules (e.g. BMP4 and WNT2B) that were able to maintain cancer stem cell niche, complements (e.g. C1S and C3) and chemokines (e.g. CCL2, CXCL12 and CXCL14) that regulated tumor immunity and inflammation. The ECM-remodeling CAFs highly expressed abundant extracellular matrix (ECM) proteins (such as ECM collagens and fibronectin), strongly associated with a fibrotic matrix (Fig. 4c). They also expressed a large number of ECM proteases, which altered ECM and assisted angiogenesis and metastasis (Koliaraki et al., 2017). The contractile CAFs enriched for genes involved in regulation of cell contraction (Fig. 4c), suggesting some distinct phenotypes. Since CAFs have numerous potential cellular sources, we suggested the cluster 4 tended to be myofibroblast nature for their upregulation of myofibroblast markers (e.g. ACTA2 and TAGLN) and genes involved in myogenesis (e.g. MYH11, PLN and CNN1) (Elyada et al., 2019; Koliaraki et al., 2017). Cluster 5, highly expressing pericyte-associated markers (e.g. RGS5 and CSPG4), were largely pericytes source (Koliaraki et al., 2017). Cluster 3 upregulate genes involved in stress response (e.g., JUN, BAG3 and HSPA2) and only present in liver metastases, suggesting they may be triggered as adaptation to tumor microenvironments.

CAFs derived from treated and untreated tumor exhibited distinct phenotypes (Fig. 4b, right panel). ECM-remodeling CAFs were prevalent in the primary CRC in treatment-naïve tumors (Fig. 4d), whereas contractile CAFs were more prevalent in tumors treated with preoperative chemotherapy both in primary (cluster 4) and liver metastases (cluster 3 and cluster 5). Secretory CAFs were observed in the primary CRC, and were mainly enriched in treated tumors (except cluster 0) (Fig. 4d). Comparison the CAFs from treatment-naive tumors and treated tumors, CAFs from treatment-naive tumors were strongly enriched for processes of ECM organization and collagen metabolism (Fig. 4e), whereas CAFs in tumors treated with PC were significantly enriched pathways involved in regulating muscle cell differentiation, immune system (T cell activation) and epithelial cell proliferation (Fig. 4e). As we know, ECM remodeling is one important feature of CAFs common to progressive tumor and promotes metastasis (Bonnans et al., 2014). The observations here indicated that preoperative chemotherapy suppressed ECM remodeling in CAFs, but promotes accumulation of myofibroblast and diverse of secretory CAFs in metastases of CRC.

5. Preoperative chemotherapy suppress the CD8 + dysfunctional T cells.

Here, we also identified different phenotypes of T cells (Fig. 5a), including naïve T cells (T_N), central memory T cells (T_{CM}), intraepithelial lymphocytes (IELs), tissue-resident memory T cells (T_{RM}) /effector

memory T cells (T_{EM}), recently activated effector memory T cells (T_{EMRA}), dysfunctional or “exhausted” T cells (T_{EX}), T_H17-like cells, CXCL13 + T_H1-like cells, MKI67 + T cells and regulatory T cells (Tregs). Within these sub-populations, T_N, T_{CM} and T_{EMRA} were mainly enriched in blood, while IELs were most exclusively populated with cells form primary cancer, T_{EX} cells and T_{RM} cells were presented both in primary and liver metastasis. The treatment state and tissue origin are mapped in Figure S4a. The annotation was confirmed by expression of canonical markers (Figure S4b, S4c and Method).

In addition, we also identified two MKI67 + CD8 + T cell populations (T36 and T24) in the T cell populations (Fig. 5b). Closer examination of those two clusters revealed cluster 36 were prevalent in the liver metastases (Fig. 5b, 96% in liver and 4% in the primary CRC), whereas cluster 24 were enriched in both the primary CRC and the liver (53% in CRC and 45% in liver), indicating that primary CRC and liver metastases share cluster 24, and the liver metastases has their specific T cells characterized by high proliferation property (T36). To identify differences of those two subpopulations of T cells, we detected differentially expressed genes (DEGs) between T24 and T36 with p-value less than 1%, log2-fold change more than l and more than 10% cells expressing the gene. The results revealed heat-shock protein genes such as HSP90AA1, HSPA6, HSPA1A, HSPA1B and DNAJA4, and some molecular chaperones (e.g. BAG3 and HSPB1) were greatly upregulated in cluster 36 (Fig. 5b). Gene ontology (GO) analysis showed that cluster 36 was mainly enriched for protein folding, and response to stress (response to temperature stimulus, response to heat, response to topologically incorrect protein), suggesting they may be activated as adaptation to tumor microenvironments.

Many studies revealed that chemotherapy could impact the compartment of T cells. For example, chemotherapy could increase TIL (tumor-infiltrating lymphocyte) infiltration and decrease Tregs accumulation and proliferation in CRC patients (Maeda et al., 2011; Terme et al., 2013). Comparison of the cellular diversity of T cells in treatment- naïve tumors and tumors treated with PC, we found most subsets of CD4 + T cell were shared in chemotherapy- treated and untreated tumors (Fig. 5c, 5d), but the phenotypes of CD8 + T cells were significantly different (Fig. 5c, 5d).

In the treatment- naïve tumors, different phenotypes of CD8 + T cell were infiltrated in the primary tumor, including effector T cells and exhausted T cells, but in the metastatic sites, for the CD8 + T cells, only dysfunctional or exhausted T cells were accumulated in the liver (Fig. 5c). Most significantly, preoperative chemotherapy suppressed accumulation of dysfunctional T cell significantly both in the niches of primary CRC and liver metastases (Fig. 5e), which were validated by immunofluorescence (Figure S5). Consistent with previous studies (Maeda et al., 2011; Terme et al., 2013), chemotherapy decrease the accumulation of Tregs in the primary CRC, but in liver metastases, the abundance of Tregs were comparable between treated and untreated tumors (Fig. 5f). The differentiation trajectories of CD8 + and CD4 + T cells (Fig. 2e, 2f, Figure S4e, S4f) also confirm the CD8 + dysfunctional T cells were most prevalent in treatment-naïve tumors, while the Tregs is shared in treated and untreated tumors.

6. Cell-cell cross-talks within the tumor microenvironments in liver metastasis of CRC

Tumor microenvironment are a complex ecosystems, the crosstalks between each cell determine tumor biology and response to therapies (Tirosh and Suvà, 2019). In order to systematically map cellular interactions especially different immune cells and mesenchymal cells in the TME of the primary CRC and metastases, and investigate the potential cellular communication which contribute to the cancer progression, metastases and immune evasion, we used CellPhoneDB v2.0.6 to study the cross-talks between stromal cells in tumor microenvironment. To visualize the cross-talks between different cells types, a chord diagram was built using the circlize package (Gu et al., 2014) in R.

Firstly, we provided a landscape of cross-talks within major stromal cell types both in the niche of the primary CRC and the liver metastases. Then based on each sub cell types annotated above, we focused on sub-cell types, investigated intercellular communications in tumors treated with preoperative chemotherapy and untreated tumors. Selected LR paired were summarized in Fig. 6. The full list of results that were unique to different tumor microenvironment were available in Supplementary Tables (Table S4).

The cross-talks within major stromal cells reveals that TAMs had the most broad cross-talks with other cells, both in the niche of primary CRC and liver metastases (Figure S6a, S6b). They displayed a rich ligands and receptors (LR) profile, broadly communicated with mesenchymal compartment (CAFs and endothelial cells), and immune compartment (including T cells, NK cells, mast cells, DCs and TAMs) in both the primary and liver metastases (Figure S6a). Comparison of the interactions in the primary CRC and liver metastases, we found that TAMs in the primary CRC communicated more frequently with CAFs than that in liver metastases, whereas the cross-talk between TAMs and DCs was greatly increased in the metastatic niche when compared with that in primary CRC (Figure S6a, S6b).

Then on the basis of the annotation above, we focused on cell subpopulations, to identify key interactions between each cell subpopulations.The cross-talks between different phenotypes of TAMs were most abundant in the TME, compared with other cell types. Subsequently, the cross-talks between sub populations of DCs, CAFs, TAMs, dysfunctional T cells and endothelial cells were relatively more frequent. Whereas immune cell such as B cell, plasma cells, other T cell subtypes (including T_{EM}, T_{RM}, T_{EMRA} and Tregs), NK cells and mast cells communicated less in TME (Figure S6c).

Interestingly, among the TAMs compartments, monocyte-derived immature TAMs, MKI67 + TAMs and M03-CXCL10 + TAMs were more activated, with more interactions with other cell types (Figure S6c), hinting that they mediate signals between diverse cell types. Moreover, compared with other T cell subtypes, we observed MKI67 + CD8 + T cells and T_{EX} displayed a rich LR profile (Figure S6c), communicated densely with mesenchymal compartment (CAFs and endothelial cells), and immune compartment, indicating their immune-modulating functions. Both the MKI67 + CD8 + T cells and MKI67 + TAMs displayed a rich LR profile, hinting cells with highly proliferation may have more cell-to-cell communication between different cell types.

Cell-Cell communications in the niches of tumors treated with and without preoperative chemotherapy

Whether preoperative chemotherapy can reprogram the interactions within stromal cells is still unclear. To investigate the effects of chemotherapy on tumor microenvironment of liver metastases of CRC, we further compared cell interaction networks between tumors treated with PC and without PC both in primary tumor and metastatic sites.

Our data reveal the phenotypes of TAMs were highly heterogeneous, and the dysfunctional T cells and ECM-remodeling CAFs were expanded in the primary CRC of treatment-naïve tumors. While in the microenvironment of tumors treated with preoperative chemotherapy, in the primary CRC, chemotherapy promoted the activation of B cells, increased the abundance of immature and less activated TAMs, and expanded the myofibroblasts.

The LR map showed that communications related to immune regulation were more frequently and broadly in the tumors treated preoperative chemotherapy (Fig. 6a). In the niche of treatment-naïve primary tumors, we found that non-PC enriched TAMs (MHC ^{high} TAMs (M20 and M23), MHC ^{low} inflammatory TAMs (M12)) and MKI67 + TAMs (M26) expressed T cell immune checkpoint ligands CD86, interacted with dysfunctional T cells and Tregs, directly inhibited T cells function (Buchbinder and Desai, 2016; Santarpia and Karachaliou, 2015) through LR pair CD86- CTLA4 (Fig. 6a, left). While in the microenvironment of primary tumors treated with preoperative chemotherapy, the interactions involved in immunomodulation were more densely: PC-enriched TAMs expressed T cell immune checkpoint ligands CD86 and CD80, interacted with dysfunctional T cells and MKI67 + T cells through LR pair CD28- CD86, CD86- CTLA4 and CD80- CTLA4. Moreover, they mediated release of chemokine CCL20 and CXCL16, recruited CXCR3 + CD8 + T cells, CCR6 + T cells and CXCR6 + T cells through CCR6-CCL20, CXCR3-CCL20 and CXCR6-CXCL16 (Fig. 6a, right).

Moreover, preoperative chemotherapy promoted the activation of B cells. In the niche of primary tumors treated with PC, B cells, MKI67 + T cells (T24) and dysfunctional T cells expressed HLA-F, and/ or HLA-DPB1, interacted with PC-enriched TAMs through HLA-F -LILRB2 and HLA-DPB1 -NRG1 (Fig. 6a, right). Importantly, PC-enriched TAMs–M0 also expressed NRG1 and immunomodulatory gene LILRB2, broadly interacted with DCs, T_{EMA} and other TAMs through HLA-F -LILRB2 and HLA-DPB1 -NRG1 (Fig. 6a, right), implying their role involved in immune regulation.

Compared with the untreated tumors, the Notch signaling was exclusively present in tumors treated with PC. The LR map in tumors treated PC showed that myofibroblasts high expressed JAG1, interacted with Notch receptors (NOTCH2, NOTCH3 and NOTCH4) on themselves and endothelial cells (Fig. 6a, right). Notch signaling could regulate myofibroblasts phenotype, tissue fibrosis (Ni et al., 2018), and macrophage differentiation and functions (Palaga et al., 2018). While in the treatment-naïve tumors, we identified pro-angiogenic interactions among ECM- remodeling CAFs, non-PC enriched TAMs and endothelial cells. MHC ^{high} TAMs (M20 and M23) and inflammatory TAMs (M12) highly expressed pro-angiogenic factor vascular endothelial growth factor A (VEGFA), activated and recruited ECM- remodeling CAFs and endothelial cells that might generate vascular networks in the microenvironment though NPR2-VEGFA (Hirano et al., 2001; Yeo et al., 2014) (Fig. 6a, left). Notably, among the TAMs compartment, highly

expression of VEGFA are found in inflammatory MHC ^{low} TAMs (M12), which interacted with lipid-associated TAMs (M14, M18 and M19), MHC ^{high} TAMs (M20 and M23) and MKI67 + TAMs (M26) through NPR2-VEGFA (Fig. 6a, left).

Additionally, in the tumors treated with preoperative chemotherapy, we found endothelial cells densely communicated with other cells in the primary tumors. They product ACKR1 (DARC), broadly interacted with dysfunctional T cells, DCs, myofibroblast and TAMs through CCL5-ACKR1, CXCL8-ACKR1, CXCL1-ACKR1 and CCL17-ACKR1 (Fig. 6a, right). ACKR1 has a crucial role in regulation leukocytes recruitment (Pruenster et al., 2009), the high expression of ACKR1 can inhibits tumorigenesis, vascularity and metastasis (Addison et al., 2004). While in untreated tumors, endothelial cells expressed immunosuppressive genes LGALS9, communicated with MKI67 + T cells (T36), MHC ^{high} TAMs (M20 and M23) and dysfunctional T cells through LGALS9- HAVCR2 (Fig. 6a, left).

In liver metastases, chemotherapy promoted the abundance of DCs and myofibroblasts, but decreased the dysfunctional T cells.

Both in tumors treated with and without PC, LAMP3 + DCs producing CD86, CD274 (PDL1) and LGALS9, interacted with dysfunctional T cells, MKI67 + T cells and Tregs through CTLA4- CD86, PDCD1-CD274 and LGALS9- HAVCR2 (Fig. 6b). While in the untreated tumors, LAMP3 + DCs also expressed CCL19 and CXCL10, recruit CCR3 + Tregs, dysfunctional T cell and MKI67 + T cells (Fig. 6b, left).

In tumors treated with PC, in line with the observations in the primary tumors, Notch signaling was also identified in the liver metastases after tumors treated with chemotherapy (Fig. 6b, left). Importantly, TNF signaling was unique present in tumors treated with PC. MKI67 + T cells (T36) expressed tumor necrosis factor (TNF) and TNFSF14, broadly interacted with immune cells (DCs and TAMs) and non-immune cells (CAFs) though TNF- TNFRSF1A, TNF- TNFRSF1B and TNFSF14- TNFRSF14 (Fig. 6b, right), which can positively regulate T cell response and contribute to the function of effector T cells in previous studies (Croft, 2009; Zhang et al., 2018).

Comparison of tumors after treatment, in treatment-naive tumors, cross-presenting DCs expressed DPP4, interacted with TAMs through CXCL2 –DPP4, CXCL10 –DPP4 and CCL3L3- DPP4 (Fig. 6b, left). DPP4 (also known as CD26) has been showed to be positive correlated with distance metastasis in colorectal cancer (Lam et al., 2014), and the high expression of DPP4 had significantly worse overall survival in CRC (Lam et al., 2014). In addition, Cross-presenting DCs also interacted with TAMs through LGALS9- HAVCR2, implying their roles in immunosuppression.

In summary, our LR interaction map highlights ACKR1, Notch signaling and molecules mediated immune regulation may contribute to the reprogramming of TME after tumors treated with preoperative chemotherapy.

Discussion

How to improve therapeutic options for patients with metastatic CRC is a core question for CRC treatment. In this study, we performed a single cell atlas of primary CRC and their matched liver metastases with 111,292 cells, provides a fundamental and comprehensive understanding of cellular composition in TME of liver metastases of CRC. More importantly, for the first time, we provided a dynamic and comprehensive stromal cell mapping to illustrate how preoperative chemotherapy reprogramed the TME of both primary CRC and matched liver metastases in CRC patients.

We find that B cells mainly existed in primary CRC. Importantly, our results indicated preoperative chemotherapy may stimulate the activation of B cells. B cells in tumors treated with PC were characterized by highly expression of Ig molecules (IgG and IgA) and MHC class II molecules, down-regulation of naïve (e.g. VPREB3) and inflammatory markers (e.g. NFKBIA). Upregulation of IgG and IgA indicated they underwent class switch recombination (CSR, also known as isotype switching), a key process in B cell activation and transformation into plasma cells when they are stimulated by antigens. The activation of B cells had also been found in the scenario of cancer immunotherapy (Cabrita et al.,2019; Hollern et al., 2019; Helmink et al. 2020). Furthermore, we identified a gene signature of activated B cells and found they were positively correlated with overall survival in the TCGA COAD cohort, especially in MSS (Fig. 2i, Fig. 2j). Thus, our results suggested that the infiltration of the switched, activated B cell may play an important role in anti-tumor response, and they could be a potential predictor of effective chemotherapy and good prognosis of CRC.

In this study, we identified 18 clusters of TAMs, and classified them into four major heterogeneous subclasses based on gene expression profiles (Fig. 3c). In the primary niche of treatment-naïve tumors, our results showed hyper-inflammatory TAMs, MMPs ^{high} TAMs and MHC ^{high} TAMs were prevalent in the primary CRC, whereas the abundance and diversity of TAMs decrease significantly after tumor treated with preoperative chemotherapy. According to previous studies, MHC ^{high} TAMs were more likely to be activated TAMs, which were distributed in peritumor part and contributed to tumor invasion and metastases, and shorter survival (Kuang et al., 2011; Wu and Zheng, 2012). Additionally, TAMs play a dominant role in tumor inflammation by facilitating angiogenesis and promoting tumor growth and metastasis (Gonzalez et al., 2018; Mantovani et al., 2017; Noy and Pollard, 2014; Pikarsky et al., 2004). The subset of inflammatory TAMs had a strong inflammatory phenotype and may contribute to tumor progression seriously. Taken together, TAMs in TME of treatment naïve tumors may be tumor-promoting. Whereas, the vision of TAMs in of tumors treated with preoperative chemotherapy were very different. We found immature TAMs and less activated TAMs were more enriched. Specially, gene signature of immature TAMs (M11) is associated with better prognosis in MSS cohort. According to recent studies, high TAMs density were closely correlated with poor survival in many cancers (Gabrilovich, 2017; Ruffell and Coussens, 2015). However, TAMs targeted therapy has not been effective yet, which may be hampered by TAMs heterogeneity and elusive molecular phenotype. Our study provided a full-scale illustration of TAMs composition and molecular characteristics, which were an important basic and resource information for TAMs targeted therapy research to inhibit and cure metastatic CRC. Our results also found preoperative chemotherapy suppressed the abundance of dysfunctional T cells and ECM-

remodeling CAFs, induced the generation of myofibroblasts. The accumulation of myofibroblasts indicated tissue injury and fibrosis related to chemotherapy.

Therefore, based on the phenotypic alteration we observed in the primary CRC treated with and without preoperative chemotherapy, we suggested that chemotherapy destroyed tumor cells, which released tumor antigens and activated immune microenvironment (Fig. 7), including B cell maturation and antibody generation. Moreover, chemotherapy inhibited the diversity of TAMs and remolded the character of TAMs, which transformed into an immature and less activated phenotype. While the TME of liver metastasis displayed clearly different scenario, the number of B cells in the liver metastasis had a significant reduction, which might be a cause for the feasibility of liver metastasis of CRC. Similar to the situation of primary CRC, myofibroblast were aggregated in response to chemotherapy, which led to the fibrosis of liver metastasis.

Taken together, this atlas provides a fundamental reference for the complex cellular and phenotypic diversity within TME of both primary CRC and liver metastasis. Our systematic investigation of transcriptional changes and phenotypic alteration in TME at single-cell level can provide valuable insight into our understanding of therapeutic outcome. This may open up new possibilities to develop or improve therapeutic strategy to CRC.

Materials And Methods

Tumor specimens and Patient Clinical Characteristics

Primary CRC, matched liver metastases and blood sample were collected from six CRC patients with metastatic disease. All patients were classified as microsatellite-stable (MSS) with invasive adenocarcinomas and late-stage (IV) disease (Table S1). For each lesion, we collected the tissue in the core of the tumor after the surgery. Single cells were isolated from fresh tumor tissues without surface marker pre-selection. All patients underwent curative intent surgery of synchronous colectomy with liver resection. In addition, all patients who provided specimens signed an informed consent form and agreed to the specimens being used for scientific research, and more pathological and clinical information of patients see in Table S1. Among the patients, patients COL15, COL 17 and COL18 treated with preoperative chemotherapy, and the others were treatment naïve. More details could see in Table S1.

Tumor disaggregation and single cell collection

Venous blood was collected before surgery in EDTA anticoagulant tubes and used to isolate PBMC immediately. Fresh biopsies of the primary colorectal cancer and the matched liver metastases were collected at the time of surgical resection. Once the specimens were separated from body, they were processed for single cell RNA sequencing (scRNA-seq) immediately.

PBMC Isolation

Peripheral blood mononuclear cells (PBMCs) were isolated using Ficoll (TBD) solution according to manufacturer's instructions. In brief, 5ml fresh peripheral blood was layered onto equal Ficoll, following by centrifugation at 450x g for 25min. After centrifugation, lymphocytes layer remained at the plasma-Ficoll interface and were carefully transferred to a new tube and washed twice with Phosphate-Buffered Saline (PBS, ThermoFisher Scientific). Lymphocyte pellets were re-suspended with sorting buffer (Hank's Balanced Salt Solution (HBSS, ThermoFisher Scientific) with 0.04% bovine serum albumin (BSA, MRC)) for flow cytometry analyses.

Tumor Dissociation

The primary CRC and metastatic tumor tissue were dissociated using MACS® Tumor Dissociation Kit (Miltenyi Biotec). Briefly, Fresh biopsy samples of the primary and metastatic tumors were washed with Dulbecco's Phosphate-Buffered Saline (DPBS, ThermoFisher Scientific), minced into approximately 1-mm^3 pieces, and enzymatically digested with Human Tumor Dissociation Kit (Miltenyi Biotec) for 60min on a rotor at 37℃, according to the manufacturer's protocol. Cell suspension were subsequently filtered through a 40 μm Cell-Strainer (BD) and centrifuged for 10min at 400g. The supernatant was then removed, pelleted cells were suspended in red blood cell lysis buffer (Solarbio) and incubated on ice for 2min to lyse red blood cells. After washing with HBSS, the cell pellets were re-suspended in sorting buffer (HBSS with 0.04% BSA) for flow cytometry process.

Sorting of viable single cells

A single-cell suspension was stained for viability with 1μm Calcein AM (ThermoFisher Scientific) and 0.33 μM TO-PRO-3 iodide (ThermoFisher Scientific) prior to sorting. Fluorescence-activated cell sorting (FACS) was performed on BD Influx (BD Biosciences) using 488nm (calcein AM, 530/40 filter), 638nm (TO-PRO-3, 670/30 filter) lasers. Singlets were captured and doublets were discard through forward scatter height and width parameters. Viable cells were recognized as Calcein AM (high) and TO-PRO-3 (low) cell cluster. For PBMC sample, only lymphocytes and monocytes clusters were gated for further sorting. Viable single cells were resuspended in HBSS with 0.04% BSA. Viability was confirmed to be >90% using trypan blue (ThermoFisher Scientific) exclusion prior to scRNA-seq process.

Droplet-based sing-cell RNA sequencing and library preparation

The scRNA-seq libraries were constructed by using the Chromium™ Single Cell 3' Reagent Kits v2 (10x Genomics) according to manufacturer instruction. Briefly, cells were suspended in HBSS with 0.04% BSA at a concentration approximately 1000 cells/μl and appropriate suspension loading volume were

determined by calculating for a target capture 8000 cells. Cell suspension of corresponding volume were loaded onto the 10X Chromium Single Cell Platform (10X Genomics). Generation of gel beads in emulsion (GEMs), barcoding, GEM-RT clean-up, complementary DNA amplification and library construction were all performed according to manufacturer's protocol. Sequencing library quality was checked with Bioanalyzer (Agilent Bioanalyzer 2100). Library quantification was measured using Qubit before pooling. The final library pool was sequenced on the Illumina X Ten instrument using 150-base-pair paired-end reads. Sequencing data of individual sample were summarized in Table S2.

Preprocessing of single-cell RNA-seq data analysis

The raw base call (BCL) files were demultiplexed into FASTQ file by bsl2fastq. Droplet-based sequencing data were qualified by FastQC software. Then reads were aligned against GRCh38 human reference genome provided by Cell Ranger (version 2.0, 10x Genomics), unique molecular identifier (UMI) counts were summarized for each cell of each gene. The raw UMI count matrices were filtered to (1) remove cells with a low number of unique detected genes (<500); (2) for each batch, remove cells for which the total number of UMI (after $\log_{10}$ transformation) was not within the three standard deviations of the mean; (3) for each batch, remove cells that showed an unusually high or low number of genes; (4) discard cells in which the proportion of the UMI count attributable to mitochondrial genes was greater than 15%. 731 cells were filtered in step1, while step 2 to step 4 remove only a small number of cells (0.1%). After exclude low-quality cells, 25,121 protein-coding genes across 111,292 single cells remained for downstream processing.

Identification of cell types and subtypes by dimensional reduction

After quality control, raw UMI counts were lognormalized using the scale of 10,000. The genes with normalized expression between 0.0125 and 3, and dispersion >0.5 were selected as highly variable genes. 1511 highly variable genes were identified based on dispersion and mean. "var.to.regress" option UMI's and percent mitochondrial content were used to regress out unwanted sources of variation. The resultants were first summarized by principle component analysis (PCA). We used the function *FindClusters* on 50 PCs with resolution 1.0 to perform the first-round cluster and annotation. The annotation of each cell cluster was confirmed by the expression of many canonical marker genes. As shown in Figure S1b, tumor cells were identified using the higher expression of EPCAM, other cell types were annotated using: T cells (CD3D, CD3E, TRAC), B cells (CD19, CD79A, MS4A1), Plasma cells (IGHG1, IGHA1, MZB1, CD79A), Monocytes and macrophages (CD68, CD163, CD14, LYZ), NK Cells (KLRF1, KLRD1, FGFBP2, FCG3RA and PRF1). CAFs (FAP, COL1A1, COL3A1, DCN and ACTA2), Endothelial cells (CLDN5, CDH5 and VMF), pDC (LILRA4 and IL3RA) and mast cells (TPSAB1, TPSB2 and MS4A2). Then focusing on each major cell types, the same clustering protocol was used to identify clusters within the major cell types aforementioned.

Among the T cell compartments, cell types were identified using genes previous reported: Naïve T cells were identified by expressed the “naïve” marker genes such as CCR7, SELL and LEF1. T_{RMRA} were identified by expressing cytotoxic markers: KLRG1, GZMH, NKG7, and PRF1, but without upregulation of inhibitory molecules. T_H17-like cluster upregulation of IL23R and IL17A, T_{RM}-like clusters expressing markers: CD69, IL7R, CXCR4 and GPR18. T_{EM} clusters were characterized by high expression of chemokine receptor CXCR4 and mild expression of cytotoxic molecules (GZMK and IFNG). Tregs (marked by high expression of FOXP3 and IL2RA. Moreover, a small subset of cluster were characterized as intraepithelial lymphocytes (IELs) based on the highly expressed γδT cell receptors (TRGC2) and NK cell markers. Furthermore, consistent with previous results [22,34], a subset characteristic of follicular helper T cells (CXCL13+T_H1-like cells) was observed in CD4+ T cells, highly expressed CXCL13 and some inhibitory molecules (such as CTLA-4).

Pathway enrichment analysis

We used the R package limma (Ritchie et al., 2015) to identified differentially expressed genes between cells from treatment-naïve tumors and chemotherapy-treated tumors. The Benjamini–Hochberg multiple testing correction was applied to estimate the FDR.

Biological-process Gene ontology (GO) enrichment ($P<0.01$) were performed using clusterProfiler packages (version 3.9.2) with a Benjamini-Hochberg multiple testing adjustment. Gene sets with a FDR-corrected $P<0.01$ were considered to be significantly enriched.

Putative Interactions between Cell Types

We used CellPhoneDB v2.0.6 (www.cellphonedb.org) to study the crosstalk between stromal cells in tumor microenvironment. CellPhoneDB is a repository of curated receptor, ligand and their interactions to predict communicating pairs. They integrated multiple databases and account for subunit architecture for both ligands and receptors to represent heteromeric complexes accurately (Davidson et al., 2018; Efremova et al., 2019).

In brief, a count file which contained gene expression value and a meta file with the cell type annotation information were prepared as inputs to the algorithm, pairwise cell-cell interaction analyses were performed by CellphoneDB. In our data, only ligands or receptors expressed more than 10% in the given cell subpopulations were considered as the potential candidates. The interactions between subpopulations were identified: (1) random permute the label of all cells 1000 times, then determine the mean of the average receptor expression level in a cluster and the mean of the average ligand expression in their counterpart clusters. Thus, a null distribution could obtain for each ligands and receptors (LR) pairs in each pairwise comparison. (2) Calculating the proportion of the means, if the means were as or higher than the actual mean, a P value for the likelihood of cell-type specificity of a given LR complex were obtained. (3) We selected LR pairs which have significant p-value and are biologically relevant. To

visualize the crosstalk between different cells types, a chord diagram was build using the circlize package (Gu et al., 2014) in R.

TCGA data analysis

The TCGA COAD (colon adenocarcinoma) data were used to evaluate the correlation between selected gene signatures and patient survival. The gene expression data were downloaded from UCSC Xena (http://xena.ucsc.edu/), clinical data were download from the Genomic Data Common Data Portal (https://gdc-portal.ncu.nih.gov/). The statistical analysis was performed by the R package “survival”, the survival curved were filtered by *survfit* function. The feature genes used for B cell signature were based on the differentially expression genes (FDR<0.01, FC>1.5) of the B cells from tumors treated with PC versus the B cells from treatment-naïve tumors. The genes used for immature TAMs signature were DEG among all TAMs subsets.

Multicolor immunohistochemistry (IHC)

Multicolor IHC staining of formalin-fixed, paraffin-embedded (FFPE) tissues section were used to confirm the presence of novel subpopulations. Multicolor IHC staining was obtained using PANO 7-plex IHC kit (0004100100, Panovue). We detected the expression of CD3, CD8, PD-1. Each formalin-fixed, paraffin-embedded (FFPE) tissues section (4μm) was put through four sequential rounds of staining. Briefly, FFPE tissue section (4μm) were melted at 60℃ for 1 hour followed by deparaffinizing and rehydrating. Heat mediated antigen retrieval was performed in EDTA buffer pH 9 using microwave incubation. The section were blocked with blocking buffer (hydrogen peroxide) for 10 minutes. In the first round of staining, the section were stained with an anti-PD-1 mouse monoclonal antibody (ZM-0381, Zsbio). Then, they were incubated with an anti-rabbit and mouse horseradish peroxidase (HRP)-conjugated secondary antibody (0004100100, Panovue). The stained signal was further amplified using PPD 520 tyramide signal amplification (TSA) reagents through incubated with TSA diluent (0004100100, Panovue). After removing the bound antibody by a method similar to the antigen retrieval process using EDTA buffer pH 9, the same process was repeated in sequence for then following antibodies and fluorescent dyes: anti-CD8 (ZM-0508, Zsbio) /PPD560, anti-CD3 (85061, CST) /PPD690. Nuclei were stained with DAPI after all the staining had done.

Multispectral imaging

The obtain multispectral images, the stained slides were scanned using the Mantra system (Perkin Elmer), which captures the fluorescent spectra at 20-nmwavelength intervals from 420 to 720 nm with identical exposure time. The scans were combined to build a single stack image. Images of unstained and single-stained sections were used to extract the spectrum of autofluorescence of tissues and each fluorescein, respectively. The extracted images were further used to establish a spectral library required

for multispectral unmixing by InForm image analysis software (PerkinElmer). Using this spectral library, we obtained reconstructed images of sections with the autofluorescence removed.

Declarations

Data Availability

Raw data from scRNA-seq analysis have been deposited in the NCBI Gene Expression Omnibus (GEO) under accession numbers GSEXXX. Source Data for Figures and Supplementary Figures are provided within the online content of this paper.

Acknowledgements

We thank all members in the Li lab, Xing-Xing Shen and Pei Lin for discussion and comments. This work was supported by National Key R&D Program of China (2019YFA0802400), National Natural Science Foundation of China (81525020 and U1801282), the Guangzhou Science and Technology Plan Projects (Health Medical Collaborative Innovation Program of Guangzhou) (201803040019). China Postdoctoral Science Foundation (2019M663219).

Author contributions

J.M.L. designed the study. L.H.C. performed data analysis and interpretation. J.W.L., R. L., J.P. H. and Y. Q. L. performed the experiments. J.M.L., R. L., L.H.C., A.J.Z., P.H., and Y.Y.C. contributed to the clinical sample collection. W.N., Y.X.Z., and Y.Y.L., prepared the samples. L.H.C., J.W.L., and J.M.L. wrote the manuscript. All authors read and approved the final manuscript.

Declaration of interests

The authors declare no competing financial interests.

Supplementary Information

Supplemental Figures and Legends

Figure S1. Overview of the single cell atlas from primary CRC, matched liver metastases and blood samples. Related to Figure 1. **a**, tSNE of cells colored by tissue, treatment status. **b**, Feature tSNE plots of selected typical canonical markers of each of the major cell type. **c**, For each cluster, bar plots show the frequencies of cells across different tissue origin, treatment status and patient identify, and the number of each cluster.

Figure S2. The generation of activated B cells after preoperative chemotherapy. Related to Figure 2. a, Gene ontology (GO) analysis of DEGs for each of the 8 B cell clusters distributed in tissue. Selected GO terms with Benjamini-Hochberg –corrected P values <0.05 (one-sided Fisher's exact test) are shown. **b**, Feature plot show the expression levels of IGHG3 and IGHA1 across 7,454 single B cells illustrated in t-SNE plots.

Figure S3. Compositions and functions of TAMs. Related to Figure 3. a, tSNE plot of expression levels of selected genes in myeloid cells. **b**, Scatterplot of normalized mean expression of M1 and M2 signatures per cell (dot). The signature genes of M1 and M1 refer to Azizi et al., 2018. **c**, , GO terms for genes in each cluster of TAMs are shown. Differentially expressed genes with P < 0.01 and log2 (fold change) < − 1 or log2 (fold change) > 1 were used. **d**, GO analyses for genes that were differentially expressed between TAMs from tumor treated with PC versus treatment-naive tumors in the primary CRC (top) and liver Metastasis (bottom), respectively. Benjamini–Hochberg corrected P < 0.01.

Figure S4. The annotation of CAFs and the T cells. Related to Figure 5. a, tSNE of T cells colored by patient identify, tissue, treatment status, and number of UMI., **b**, Feature plots showing the expression of CD4, CD8A, CD8B and KLRF1. **c**, Heatmap showing the relative expression of T cell function-associated genes in each cell clusters. The relative expression was defined as the gene-wise (row) Z-score of normalized UMI counts (ln(UMI-per-10000+1)) across T cell subtypes. Black boxes highlight the prominent patterns defining known T cell subtypes. **d**, The expression of CD39

(ENTPD1) in CD8+ T cells. The red arrows labeled the CD8+ dysfunctional T cells. **e**,**f**, Developmental trajectory of CD8+ T cells (e) and CD4+ T cells (f) along pseudo-time in two-dimensional space. Expression of naïve markers, effector genes and markers related to dysfunctional genes on the trajectory maps. Cells are colored by the normalized UMI (unique molecular identifier) counts. Cells orders are inferred from the expression of most variable genes across all cells.

Figure S5. Immunofluorescence labelling of CD3, CD8, PD-1 and DAPI. Related to Figure 5. Nuclei are stained with DAPI. Images are maximum z-stack projections of 6 μm. Scale bar, 10 μm. (CRC: the sample from the primary CRC).

Figure S6. Cell-cell signaling networks. Related to Figure 6. a, Heatmap showing the number of cell-cell interactions within major cell types (T cells, B cells, plasma cells, NK cells, mast cells, CAFs, endothelial cells, TAMs and DCs). **b**, Network visualization of cell crosstalk in primary CRC and liver metastases. Colored lines indicate predicted ligand and receptor pairs among different cell types. **c**, Heatmap showing

the number of all possible cell-cell interactions within cell sub populations, based on the predication of Cellphone DB. The cell classification was based on the annotation above.

References

1. Adam, R., Delvart, V., Pascal, G., Valeanu, A., Castaing, D., Azoulay, D., Giacchetti, S., Paule, B., Kunstlinger, F., Ghémard, O., et al. (2004). Rescue surgery for unresectable colorectal liver metastases downstaged by chemotherapy: a model to predict long-term survival. Ann. Surg. *240*, 644 – 57; discussion 657-8.
2. Addison, C.L., Belperio, J.A., Burdick, M.D., and Strieter, R.M. (2004). Overexpression of the duffy antigen receptor for chemokines (DARC) by NSCLC tumor cells results in increased tumor necrosis. BMC Cancer *4*, 28.
3. Azizi, E., Carr, A.J., Plitas, G., Cornish, A.E., Konopacki, C., Prabhakaran, S., Nainys, J., Wu, K., Kiseliovas, V., Setty, M., et al. (2018). Single-Cell Map of Diverse Immune Phenotypes in the Breast Tumor Microenvironment. Cell *174*, 1293–1308.e36.
4. Bian, S., Hou, Y., Zhou, X., Li, X., Yong, J., Wang, Y., Wang, W., Yan, J., Hu, B., Guo, H., et al. (2018). Single-cell multiomics sequencing and analyses of human colorectal cancer. Science *362*, 1060–1063.
5. Bonnans, C., Chou, J., and Werb, Z. (2014). Remodelling the extracellular matrix in development and disease. Nat. Rev. Mol. Cell Biol. *15*, 786–801.
6. Brandi, G. (2016). Adjuvant chemotherapy for resected colorectal cancer metastases: Literature review and meta-analysis. World J. Gastroenterol. *22*, 519.
7. Buchbinder, E.I., and Desai, A. (2016). CTLA-4 and PD-1 Pathways: Similarities, Differences, and Implications of Their Inhibition. Am. J. Clin. Oncol. *39*, 98–106.
8. Buckley, C.D. (2019). Macrophages form a protective cellular barrier in joints. Nature *572*, 590–592.
9. Butler, A., Hoffman, P., Smibert, P., Papalexi, E., and Satija, R. (2018). Integrating single-cell transcriptomic data across different conditions, technologies, and species. Nat. Biotechnol. *36*, 411–420.
10. Cabrita, R., Lauss, M., Sanna, A., Donia, M., Skaarup Larsen, M., Mitra, S., Johansson, I., Phung, B., Harbst, K., Vallon-Christersson, J., et al. (2020). Tertiary lymphoid structures improve immunotherapy and survival in melanoma. Nature *577*, 561–565.
11. Cameron, A.M. (2017). Current Surgical Therapy. Ann. Surg. 1.
12. Cassetta, L., Fragkogianni, S., Sims, A.H., Swierczak, A., Forrester, L.M., Zhang, H., Soong, D.Y.H., Cotechini, T., Anur, P., Lin, E.Y., et al. (2019). Human Tumor-Associated Macrophage and Monocyte Transcriptional Landscapes Reveal Cancer-Specific Reprogramming, Biomarkers, and Therapeutic Targets. Cancer Cell *35*, 588–602.e10.
13. Chevrier, S., Levine, J.H., Zanotelli, V.R.T., Silina, K., Schulz, D., Bacac, M., Ries, C.H., Ailles, L., Jewett, M.A.S., Moch, H., et al. (2017). An Immune Atlas of Clear Cell Renal Cell Carcinoma. Cell *169*, 736–

749.e18.

14. Chung, W., Eum, H.H., Lee, H.-O., Lee, K.-M., Lee, H.-B., Kim, K.-T., Ryu, H.S., Kim, S., Lee, J.E., Park, Y.H., et al. (2017). Single-cell RNA-seq enables comprehensive tumour and immune cell profiling in primary breast cancer. Nat. Commun. *8*, 15081.
15. Croft, M. (2009). The role of TNF superfamily members in T-cell function and diseases. Nat. Rev. Immunol. *9*, 271–285.
16. Van Cutsem, E., Nordlinger, B., and Cervantes, A. (2010). Advanced colorectal cancer: ESMO Clinical Practice Guidelines for treatment. Ann. Oncol. *21*, v93–v97.
17. Dumitru, C.A., Moses, K., Trellakis, S., Lang, S., and Brandau, S. (2012). Neutrophils and granulocytic myeloid-derived suppressor cells: immunophenotyping, cell biology and clinical relevance in human oncology. Cancer Immunol. Immunother. *61*, 1155–1167.
18. Elyada, E., Bolisetty, M., Laise, P., Flynn, W.F., Courtois, E.T., Burkhart, R.A., Teinor, J.A., Belleau, P., Biffi, G., Lucito, M.S., et al. (2019). Cross-Species Single-Cell Analysis of Pancreatic Ductal Adenocarcinoma Reveals Antigen-Presenting Cancer-Associated Fibroblasts. Cancer Discov. *9*, 1102–1123.
19. Engblom, C., Pfirschke, C., and Pittet, M.J. (2016). The role of myeloid cells in cancer therapies. Nat. Rev. Cancer. *16 (7)*, 447–462.
20. Gabrilovich, D.I. (2017). Myeloid-Derived Suppressor Cells. Cancer Immunol. Res. *5*, 3–8.
21. Gelse, K., Pöschl, E., and Aigner, T. (2003). Collagens–structure, function, and biosynthesis. Adv. Drug Deliv. Rev. *55*, 1531–1546.
22. Glimelius, B., Tiret, E., Cervantes, A., Arnold, D., and ESMO Guidelines Working Group (2013). Rectal cancer: ESMO Clinical Practice Guidelines for diagnosis, treatment and follow-up. Ann. Oncol. Off. J. Eur. Soc. Med. Oncol. *24 Suppl 6*, vi81-8.
23. Gonzalez, H., Hagerling, C., and Werb, Z. (2018). Roles of the immune system in cancer: from tumor initiation to metastatic progression. Genes Dev. *32*, 1267–1284.
24. Gu, Z., Gu, L., Eils, R., Schlesner, M., and Brors, B. (2014). circlize implements and enhances circular visualization in R. Bioinformatics *30*, 2811–2812.
25. Guo, X., Zhang, Y., Zheng, L., Zheng, C., Song, J., Zhang, Q., Kang, B., Liu, Z., Jin, L., Xing, R., et al. (2018). Global characterization of T cells in non-small-cell lung cancer by single-cell sequencing. Nat. Med. *24*, 978–985.
26. Hackl, C., Neumann, P., Gerken, M., Loss, M., Klinkhammer-Schalke, M., and Schlitt, H.J. (2014). Treatment of colorectal liver metastases in Germany: a ten-year population-based analysis of 5772 cases of primary colorectal adenocarcinoma. BMC Cancer *14*, 810.
27. Helmink, B.A., Reddy, S.M., Gao, J., Zhang, S., Basar, R., Thakur, R., Yizhak, K., Sade-Feldman, M., Blando, J., Han, G., et al. (2020). B cells and tertiary lymphoid structures promote immunotherapy response. Nature *577*, 549–555.

28. Hirano, H., Tanioka, K., Yokoyama, S., Akiyama, S., and Kuratsu, J. (2001). Angiogenic effect of thymidine phosphorylase on macrophages in glioblastoma multiforme. J. Neurosurg. *95*, 89–95.
29. Hollern, D.P., Xu, N., Thennavan, A., Glodowski, C., Garcia-Recio, S., Mott, K.R., He, X., Garay, J.P., Carey-Ewend, K., Marron, D., et al. (2019). B Cells and T Follicular Helper Cells Mediate Response to Checkpoint Inhibitors in High Mutation Burden Mouse Models of Breast Cancer. Cell *179*, 1191–1206.e21.
30. Jaitin, D.A., Adlung, L., Thaiss, C.A., Weiner, A., Li, B., Descamps, H., Lundgren, P., Bleriot, C., Liu, Z., Deczkowska, A., et al. (2019). Lipid-Associated Macrophages Control Metabolic Homeostasis in a Trem2-Dependent Manner. Cell *178*, 686–698.e14.
31. Jemal, A., Bray, F., Center, M.M., Ferlay, J., Ward, E., and Forman, D. (2011). Global cancer statistics. CA. Cancer J. Clin. *61*, 69–90.
32. Kapiteijn, E., Marijnen, C.A.M., Nagtegaal, I.D., Putter, H., Steup, W.H., Wiggers, T., Rutten, H.J.T., Pahlman, L., Glimelius, B., van Krieken, J.H., et al. (2001). Preoperative radiotherapy combined with total mesorectal excision for resectable rectal cancer. N. Engl. J. Med. *345*, 638–646.
33. Koliaraki, V., Pallangyo, C.K., Greten, F.R., and Kollias, G. (2017). Mesenchymal Cells in Colon Cancer. Gastroenterology *152*, 964–979.
34. Kuang, D.-M., Zhao, Q., Wu, Y., Peng, C., Wang, J., Xu, Z., Yin, X.-Y., and Zheng, L. (2011). Peritumoral neutrophils link inflammatory response to disease progression by fostering angiogenesis in hepatocellular carcinoma. J. Hepatol. *54*, 948–955.
35. Lam, C.S.-C., Cheung, A.H.-K., Wong, S.K.-M., Wan, T.M.-H., Ng, L., Chow, A.K.-M., Cheng, N.S.-M., Pak, R.C.-H., Li, H.-S., Man, J.H.-W., et al. (2014). Prognostic significance of CD26 in patients with colorectal cancer. PLoS One *9*, e98582.
36. Lambrechts, D., Wauters, E., Boeckx, B., Aibar, S., Nittner, D., Burton, O., Bassez, A., Decaluwé, H., Pircher, A., Van den Eynde, K., et al. (2018). Phenotype molding of stromal cells in the lung tumor microenvironment. Nat. Med. *24*, 1277–1289.
37. Lavin, Y., Kobayashi, S., Leader, A., Amir, E.D., Elefant, N., Bigenwald, C., Remark, R., Sweeney, R., Becker, C.D., Levine, J.H., et al. (2017). Innate Immune Landscape in Early Lung Adenocarcinoma by Paired Single-Cell Analyses. Cell *169*, 750–765.e17.
38. Lee, J.W., Mok, H.J., Lee, D.Y., Park, S.C., Kim, G.-S., Lee, S.-E., Lee, Y.-S., Kim, K.P., and Kim, H.D. (2017). UPLC-QqQ/MS-Based Lipidomics Approach To Characterize Lipid Alterations in Inflammatory Macrophages. J. Proteome Res. *16*, 1460–1469.
39. Leung, M.L., Davis, A., Gao, R., Casasent, A., Wang, Y., Sei, E., Vilar, E., Maru, D., Kopetz, S., and Navin, N.E. (2017). Single-cell DNA sequencing reveals a late-dissemination model in metastatic colorectal cancer. Genome Res. *27*, 1287–1299.
40. Li, H., Courtois, E.T., Sengupta, D., Tan, Y., Chen, K.H., Goh, J.J.L., Kong, S.L., Chua, C., Hon, L.K., Tan, W.S., et al. (2017). Reference component analysis of single-cell transcriptomes elucidates cellular heterogeneity in human colorectal tumors. Nat. Genet. *49*, 708–718.

41. Li, H., van der Leun, A.M., Yofe, I., Lubling, Y., Gelbard-Solodkin, D., van Akkooi, A.C.J., van den Braber, M., Rozeman, E.A., Haanen, J.B.A.G., Blank, C.U., et al. (2019). Dysfunctional CD8 T Cells Form a Proliferative, Dynamically Regulated Compartment within Human Melanoma. Cell *176*, 775–789.e18.
42. Lise, M., Pilati, P., Da Pian, P., Mocellin, S., Nitti, D., and Corazzino, S. (2003). Treatment Options for Liver Metastases from Colorectal Cancer. J. Exp. Clin. Cancer Res. *22*, 149–156.
43. Maeda, K., Hazama, S., Tokuno, K., Kan, S., Maeda, Y., Watanabe, Y., Kamei, R., Shindo, Y., Maeda, N., Yoshimura, K., et al. (2011). Impact of chemotherapy for colorectal cancer on regulatory T-cells and tumor immunity. Anticancer Res.
44. Mantovani, A., Marchesi, F., Malesci, A., Laghi, L., and Allavena, P. (2017). Tumour-associated macrophages as treatment targets in oncology. Nat. Rev. Clin. Oncol. *14*, 399–416.
45. Miller, K.D., Nogueira, L., Mariotto, A.B., Rowland, J.H., Yabroff, K.R., Alfano, C.M., Jemal, A., Kramer, J.L., and Siegel, R.L. (2019). Cancer treatment and survivorship statistics, 2019. CA. Cancer J. Clin. *69*, 363–385.
46. Müller, S., Kohanbash, G., Liu, S.J., Alvarado, B., Carrera, D., Bhaduri, A., Watchmaker, P.B., Yagnik, G., Di Lullo, E., Malatesta, M., et al. (2017). Single-cell profiling of human gliomas reveals macrophage ontogeny as a basis for regional differences in macrophage activation in the tumor microenvironment. Genome Biol. *18*, 234.
47. Ngambenjawong, C., Gustafson, H.H., and Pun, S.H. (2017). Progress in tumor-associated macrophage (TAM)-targeted therapeutics. Adv. Drug Deliv. Rev. *114*, 206–221.
48. Ni, M., Wang, Y., Wu, W., Xia, C., Zhang, Y., Xu, J., Xu, T., and Li, J. (2018). Novel Insights on Notch signaling pathways in liver fibrosis. Eur. J. Pharmacol. *826*, 66–74.
49. Nordlinger, B., Guiguet, M., Vaillant, J.C., Balladur, P., Boudjema, K., Bachellier, P., and Jaeck, D. (1996). Surgical resection of colorectal carcinoma metastases to the liver. A prognostic scoring system to improve case selection, based on 1568 patients. Association Française de Chirurgie. Cancer *77*, 1254–1262.
50. Nordlinger, B., Sorbye, H., Glimelius, B., Poston, G.J., Schlag, P.M., Rougier, P., Bechstein, W.O., Primrose, J.N., Walpole, E.T., Finch-Jones, M., et al. (2008). Perioperative chemotherapy with FOLFOX4 and surgery versus surgery alone for resectable liver metastases from colorectal cancer (EORTC Intergroup trial 40983): a randomised controlled trial. Lancet (London, England) *371*, 1007–1016.
51. Noy, R., and Pollard, J.W. (2014). Tumor-Associated Macrophages: From Mechanisms to Therapy. Immunity. *41*(*1*), 49–61.
52. Palaga, T., Wongchana, W., and Kueanjinda, P. (2018). Notch signaling in macrophages in the context of cancer immunity. Front. Immunol. *9*, 652.
53. Petitprez, F., de Reyniès, A., Keung, E.Z., Chen, T.W.W., Sun, C.M., Calderaro, J., Jeng, Y.M., Hsiao, L.P., Lacroix, L., Bougoüin, A., et al. (2020). B cells are associated with survival and immunotherapy response in sarcoma. Nature *577*, 556–560.

54. Pikarsky, E., Porat, R.M., Stein, I., Abramovitch, R., Amit, S., Kasem, S., Gutkovich-Pyest, E., Uriell-Shoval, S., Galun, E., and Ben-Neriah, Y. (2004). NF-κB functions as a tumour promoter in inflammation-associated cancer. Nature. *431*,461–466.
55. Pruenster, M., Mudde, L., Bombosi, P., Dimitrova, S., Zsak, M., Middleton, J., Richmond, A., Graham, G.J., Segerer, S., Nibbs, R.J.B., et al. (2009). The Duffy antigen receptor for chemokines transports chemokines and supports their promigratory activity. Nat. Immunol. *10*, 101–108.
56. Puram, S. V., Tirosh, I., Parikh, A.S., Patel, A.P., Yizhak, K., Gillespie, S., Rodman, C., Luo, C.L., Mroz, E.A., Emerick, K.S., et al. (2017). Single-Cell Transcriptomic Analysis of Primary and Metastatic Tumor Ecosystems in Head and Neck Cancer. Cell *171*, 1611–1624.e24.
57. Ritchie, M.E., Phipson, B., Wu, D., Hu, Y., Law, C.W., Shi, W., and Smyth, G.K. (2015). limma powers differential expression analyses for RNA-sequencing and microarray studies. Nucleic Acids Res. *43*, e47–e47.
58. Roerink, S.F., Sasaki, N., Lee-Six, H., Young, M.D., Alexandrov, L.B., Behjati, S., Mitchell, T.J., Grossmann, S., Lightfoot, H., Egan, D.A., et al. (2018). Intra-tumour diversification in colorectal cancer at the single-cell level. Nature *556*, 457–462.
59. Ruffell, B., and Coussens, L.M. (2015). Macrophages and Therapeutic Resistance in Cancer. Cancer Cell *27*, 462–472.
60. Santarpia, M., and Karachaliou, N. (2015). Tumor immune microenvironment characterization and response to anti-PD-1 therapy. Cancer Biol. Med. *12*, 74–78.
61. Savas, P., Virassamy, B., Ye, C., Salim, A., Mintoff, C.P., Caramia, F., Salgado, R., Byrne, D.J., Teo, Z.L., Dushyanthen, S., et al. (2018). Single-cell profiling of breast cancer T cells reveals a tissue-resident memory subset associated with improved prognosis. Nat. Med. *24*, 986–993.
62. Siegel, R., Naishadham, D., and Jemal, A. (2012). Cancer statistics, 2012. CA. Cancer J. Clin. *62*, 10–29.
63. Stuart, T., Butler, A., Hoffman, P., Hafemeister, C., Papalexi, E., Mauck, W.M., Hao, Y., Stoeckius, M., Smibert, P., and Satija, R. (2019). Comprehensive Integration of Single-Cell Data. Cell *177*, 1888–1902.e21.
64. Tauriello, D.V.F., Calon, A., Lonardo, E., and Batlle, E. (2017). Determinants of metastatic competency in colorectal cancer. Mol. Oncol. *11*, 97–119.
65. Terme, M., Pernot, S., Marcheteau, E., Sandoval, F., Benhamouda, N., Colussi, O., Dubreuil, O., Carpentier, A.F., Tartour, E., and Taieb, J. (2013). VEGFA-VEGFR pathway blockade inhibits tumor-induced regulatory T-cell proliferation in colorectal cancer. Cancer Res. *73*, 539–549.
66. Tirosh, I., and Suvà, M.L. (2019). Deciphering Human Tumor Biology by Single-Cell Expression Profiling. Annu. Rev. Cancer Biol. *3*, 151–166.
67. Tirosh, I., Izar, B., Prakadan, S.M., Wadsworth, M.H., Treacy, D., Trombetta, J.J., Rotem, A., Rodman, C., Lian, C., Murphy, G., et al. (2016). Dissecting the multicellular ecosystem of metastatic melanoma by single-cell RNA-sEq. Science *352*, 189–196.

68. Vatandoust, S. (2015). Colorectal cancer: Metastases to a single organ. World J. Gastroenterol. *21*, 11767.
69. Wagner, J., Rapsomaniki, M.A., Chevrier, S., Anzeneder, T., Langwieder, C., Dykgers, A., Rees, M., Ramaswamy, A., Muenst, S., Soysal, S.D., et al. (2019). A Single-Cell Atlas of the Tumor and Immune Ecosystem of Human Breast Cancer. Cell *177*, 1330–1345.e18.
70. Wolock, S.L., Lopez, R., and Klein, A.M. (2019). Scrublet: Computational Identification of Cell Doublets in Single-Cell Transcriptomic Data. Cell Syst.
71. Wu, Y., and Zheng, L. (2012). Dynamic Education of Macrophages in Different Areas of Human Tumors. Cancer Microenviron. *5*, 195–201.
72. Yeo, E.J., Cassetta, L., Qian, B.Z., Lewkowich, I., Li, J.F., Stefater, J.A., Smith, A.N., Wiechmann, L.S., Wang, Y., Pollard, J.W., et al. (2014). Myeloid wnt7b mediates the angiogenic switch and metastasis in breast cancer. Cancer Res.
73. Yost, K.E., Satpathy, A.T., Wells, D.K., Qi, Y., Wang, C., Kageyama, R., McNamara, K.L., Granja, J.M., Sarin, K.Y., Brown, R.A., et al. (2019). Clonal replacement of tumor-specific T cells following PD-1 blockade. Nat. Med. *25*, 1251–1259.
74. Zhang, L., Yu, X., Zheng, L., Zhang, Y., Li, Y., Fang, Q., Gao, R., Kang, B., Zhang, Q., Huang, J.Y., et al. (2018). Lineage tracking reveals dynamic relationships of T cells in colorectal cancer. Nature *564*, 268–272.
75. Zhang, Q., He, Y., Luo, N., Patel, S.J., Han, Y., Gao, R., Modak, M., Carotta, S., Haslinger, C., Kind, D., et al. (2019a). Landscape and Dynamics of Single Immune Cells in Hepatocellular Carcinoma. Cell *179*, 829–845.e20.
76. Zhang, Y., Zheng, L., Zhang, L., Hu, X., Ren, X., and Zhang, Z. (2019b). Deep single-cell RNA sequencing data of individual T cells from treatment-naïve colorectal cancer patients. Sci. Data *6*, 131.
77. Zhen, A., Krutzik, S.R., Levin, B.R., Kasparian, S., Zack, J.A., and Kitchen, S.G. (2014). CD4 Ligation on Human Blood Monocytes Triggers Macrophage Differentiation and Enhances HIV Infection. J. Virol. *88*, 9934–9946.
78. Zheng, C., Zheng, L., Yoo, J.-K., Guo, H., Zhang, Y., Guo, X., Kang, B., Hu, R., Huang, J.Y., Zhang, Q., et al. (2017). Landscape of Infiltrating T Cells in Liver Cancer Revealed by Single-Cell Sequencing. Cell *169*, 1342–1356.e16.
79. Zheng, Y., Lilo, S., Brodsky, I.E., Zhang, Y., Medzhitov, R., Marcu, K.B., and Bliska, J.B. (2011). A Yersinia effector with enhanced inhibitory activity on the NF-κB pathway activates the NLRP3/ASC/caspase-1 inflammasome in macrophages. PLoS Pathog. *7*, e1002026.

Figures

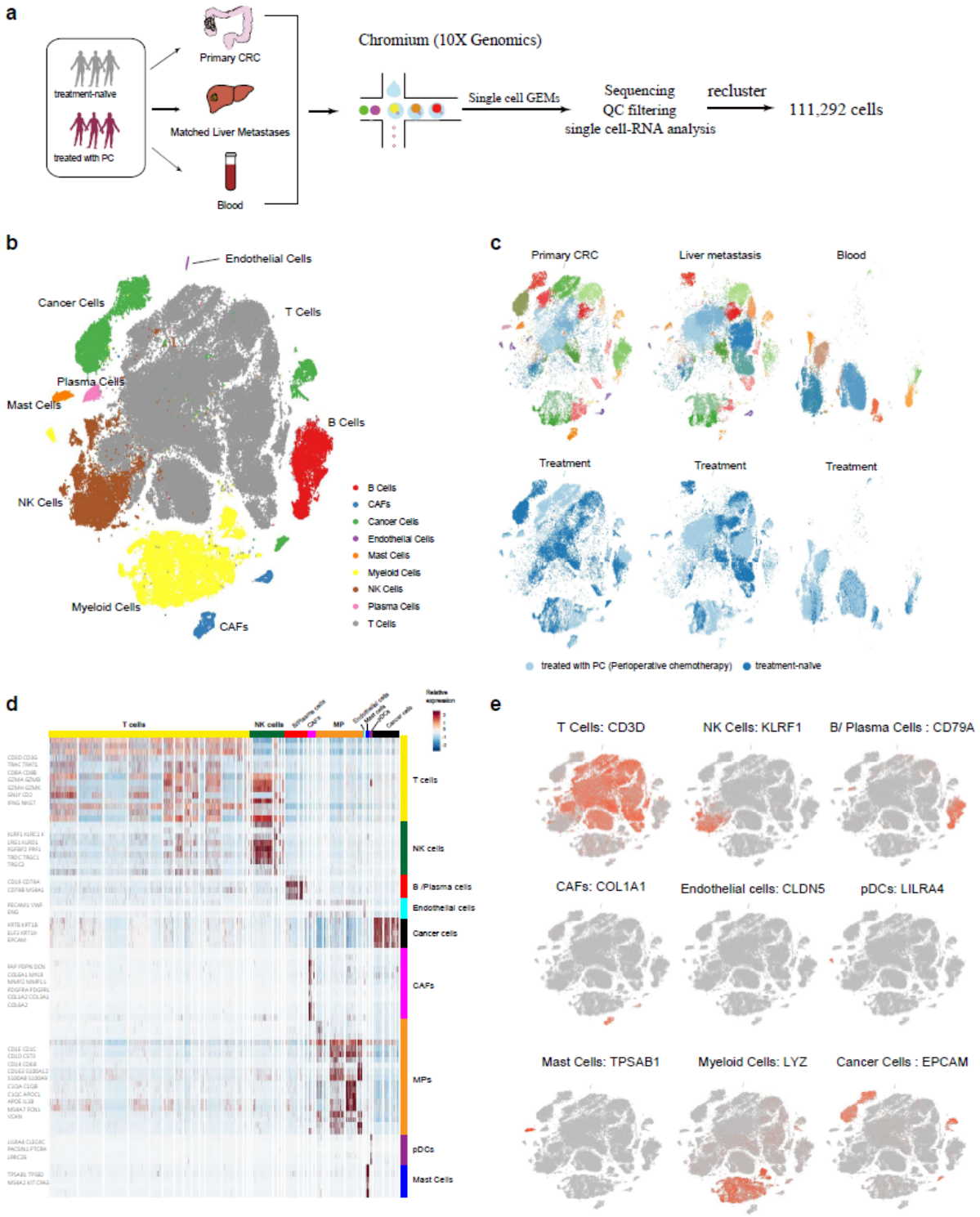

Figure 1

Single cell atlas of liver metastases of colorectal cancer. a, Overview of the workflow for single-cell transcriptome profiling of cells in primary CRC, matched liver metastases and blood. b, tSNE plot showing the landscape of 111,292 stromal cells from six liver metastases of CRC patients, visualized by tSNE. Colour indicate cell types. c, tSNE plot showing the stromal cells colored by tissue (top) and treatment status (bottom). d, Heat map showing differential expression of the top expressed genes in each cluster.

For each cluster, the top 10 genes and their relative expression are shown. (MPs, mononuclear phagocytes; pDCs, plasmacytoid dendritic cells.) e, Feature tSNE plots of typical canonical markers of each of the major cell type.

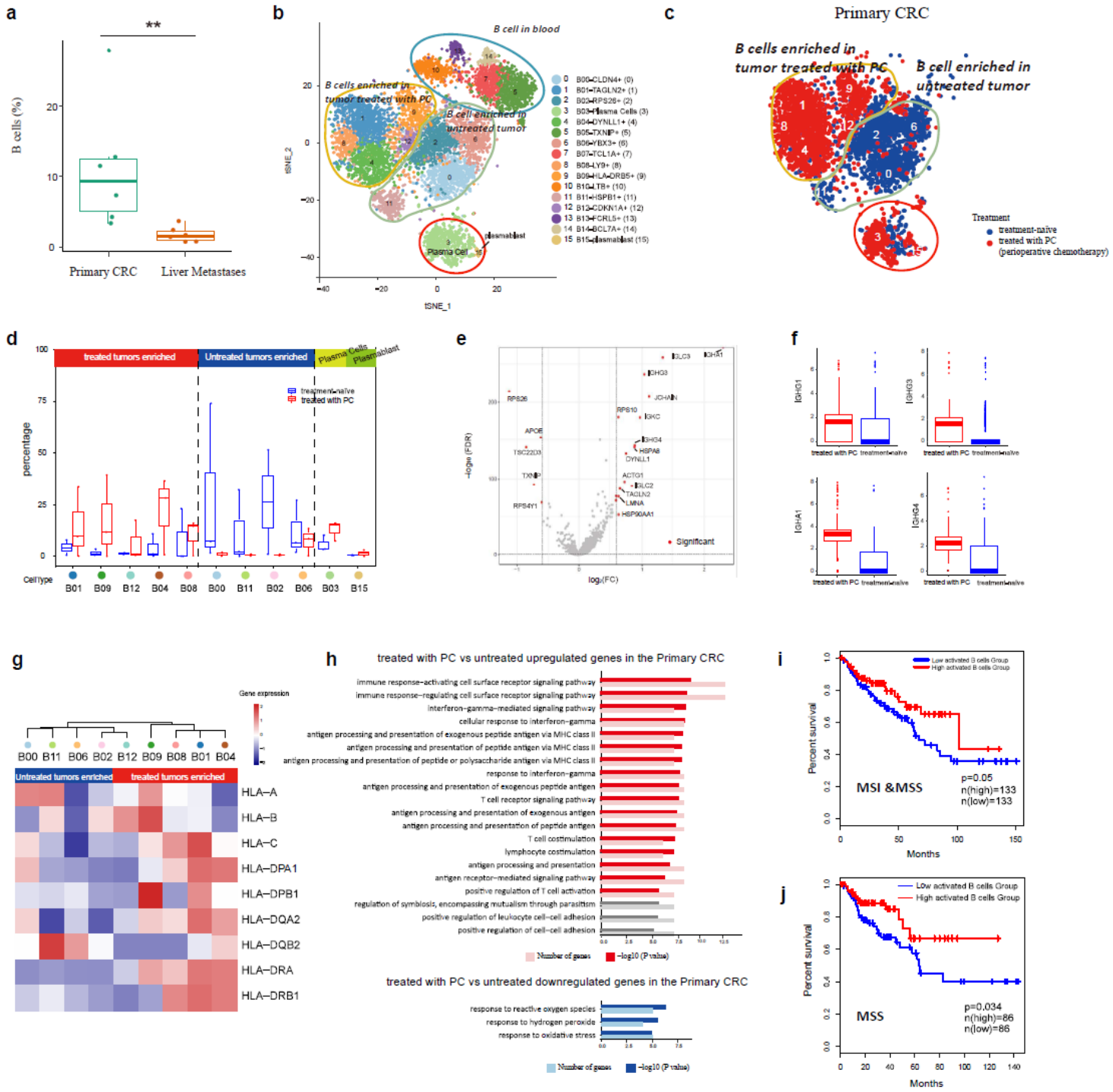

Figure 2

scRNA-seq of B cells reveals distinct cell type subpopulations in tumors treated with preoperative chemotherapy and treatment-naïve. a, Boxplots comparing the frequency of B cells in each patient in the primary CRC and liver metastases respectively. Each dot represents the percentage of B cells from one

sample, P value were calculated using Wilcoxon rank-sum test, *p <0.05, **p < 0.01. b, tSNE plot of scRNA-seq profile from 7,454 B cells separated into 17 subtypes. Cells are colored by different cell types. c, tSNE plot of scRNA-seq profile from B cells in the primary CRC. Cells are colored by treatment status (treated with PC or without PC). d, Boxplots showing the frequencies of each B cell sub cluster in untreated and treated samples in the primary CRC. The plot show B01, B10, B13, B14 and B09 enriched in tumors treated with PC, while B00, B12, B02 and B06 prevalent in untreated tumors. e, Volcano plot showing differentially expressed genes between B cells enriched in tumors treated with PC and B cells prevalent in untreated tumors. Each red dot denotes an individual gene with adjusted P value <0.05 and fold change≥1.5 (two-sided moderated t-test with limma). f, Box plots shows the expression of IGHG1, IGHG3, IGHG4 and IGHA1 in tumors treated with preoperative chemotherapy and treatment- naïve tumors. g, Heatmap showed the relative expression of MHC molecules in each B cell subtype. h, GO analysis for differentially upregulated genes and downregulated genes with P <0.05 for tumors treated with PC versus without PC. Pathways related to immune activation signaling are colored by red, pathways related to inflammation are colored by blue. i, The Kaplan-Meier overall survival curves of TCGA COAD patients grouped by the gene signature of DEG unregulated in B cells treated with preoperative chemotherapy. while the patients used in analyses including MSI-high, MSI-low and MSS patients. The B cell gene signature significant separated patients into high- (n=133 patients) and low groups (n=133 patients) with different survival time with the P values = 0.05. j. Overall survival curved of TCGA COAD data, while the patients used in analyses only including MSS patients, the P values = 0.034.

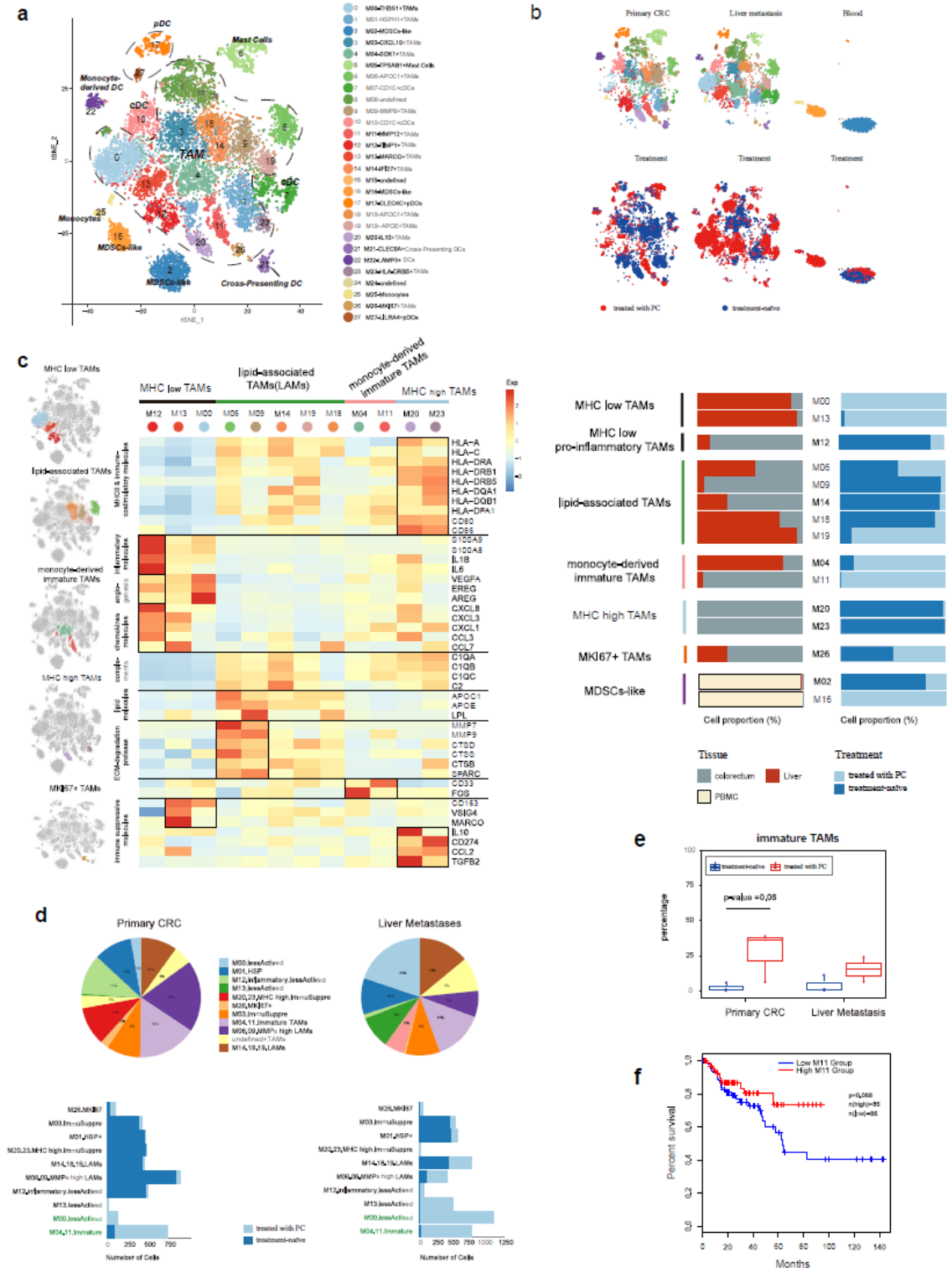

Figure 3

The phenotypic heterogeneity of myeloid cells. a, tSNE plot showing a total of 15,366 myeloid cells, separated into 28 subtypes. b, Cells are colored by tissue origin (top) and treatment status (bottom). c, Heat map showing normalized expression (z-score) of function-associated genes in TAM subsets. Black boxes highlight the prominent patterns defining TAMs cell subtypes, and bar plot show the tissue origin and treatment status of each TAM. d, Based on the annotation and classification above, the bar plot

depicting the number of cells in each cell type for different treatment status for scRNA-seq profiles. Pie charts showing the proportions of different TAM subsets within different tissues (the primary CRC, liver metastases and blood). e, Boxplot comparing the frequency of immature TAMs in each patient in the primary CRC and liver metastases respectively. Wilcoxon rank-sum test was used for statistical analysis. *p < 0.05, **p < 0.01, ***p < 0.001. f, Overall survival curves of TCGA COAD patients (Cox regression). M11 TAMs signatures were based on DEGs among all TAMs subsets (Top Rank ≤25).

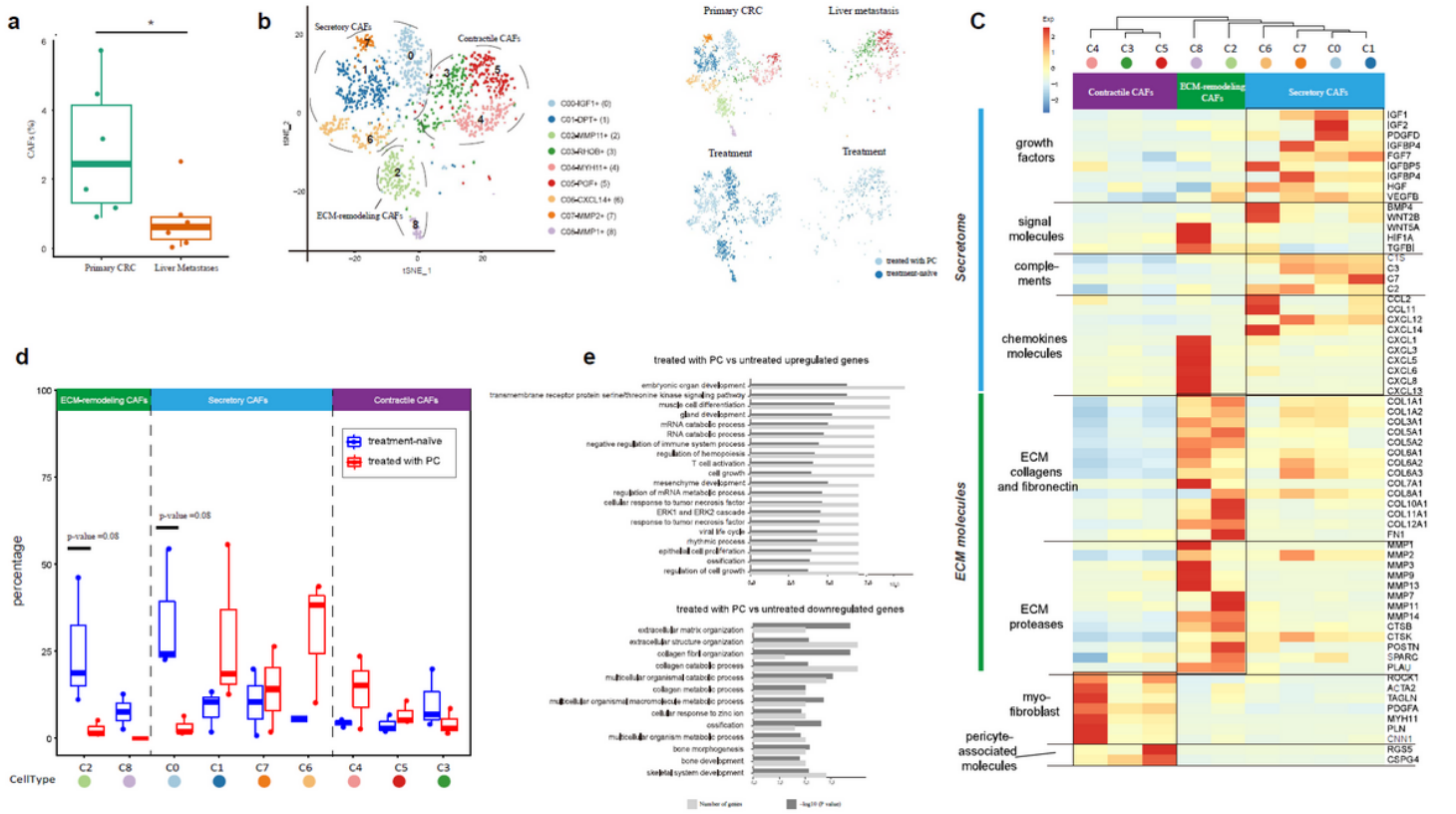

Figure 4

Compositions and phenotypes of CAF in liver metastases of CRC. a, The percentage of CAFs cells in six primary CRC and six matched liver metastases sample from six CRC patients with liver metastatic disease. Each dot represents cells from one sample, *P = 0.031, using two-sides Wilcoxon rank-sum test. b, tSNE plot groups showing a total of 1383 cell clusters defined within fibroblast subtypes, cells are colored by different cell types (left), tissue origin (right) and treatment status (right). c, Heat map showing the selected marker genes in each cluster. Relative expression was defined as the gene-wise (row) z-score of normalized UMI counts across CAFs subtypes (column). d, Box plots showing the percentage of each CAF subtype from tumors treated with and without preoperative chemotherapy in the primary CRC. Wilcoxon rank-sum test was used for statistical analysis. e, GO analyses for genes that were differentially expressed between CAFs from tumor treated with PC versus treatment-naive tumors. Benjamini–Hochberg corrected P < 0.01.

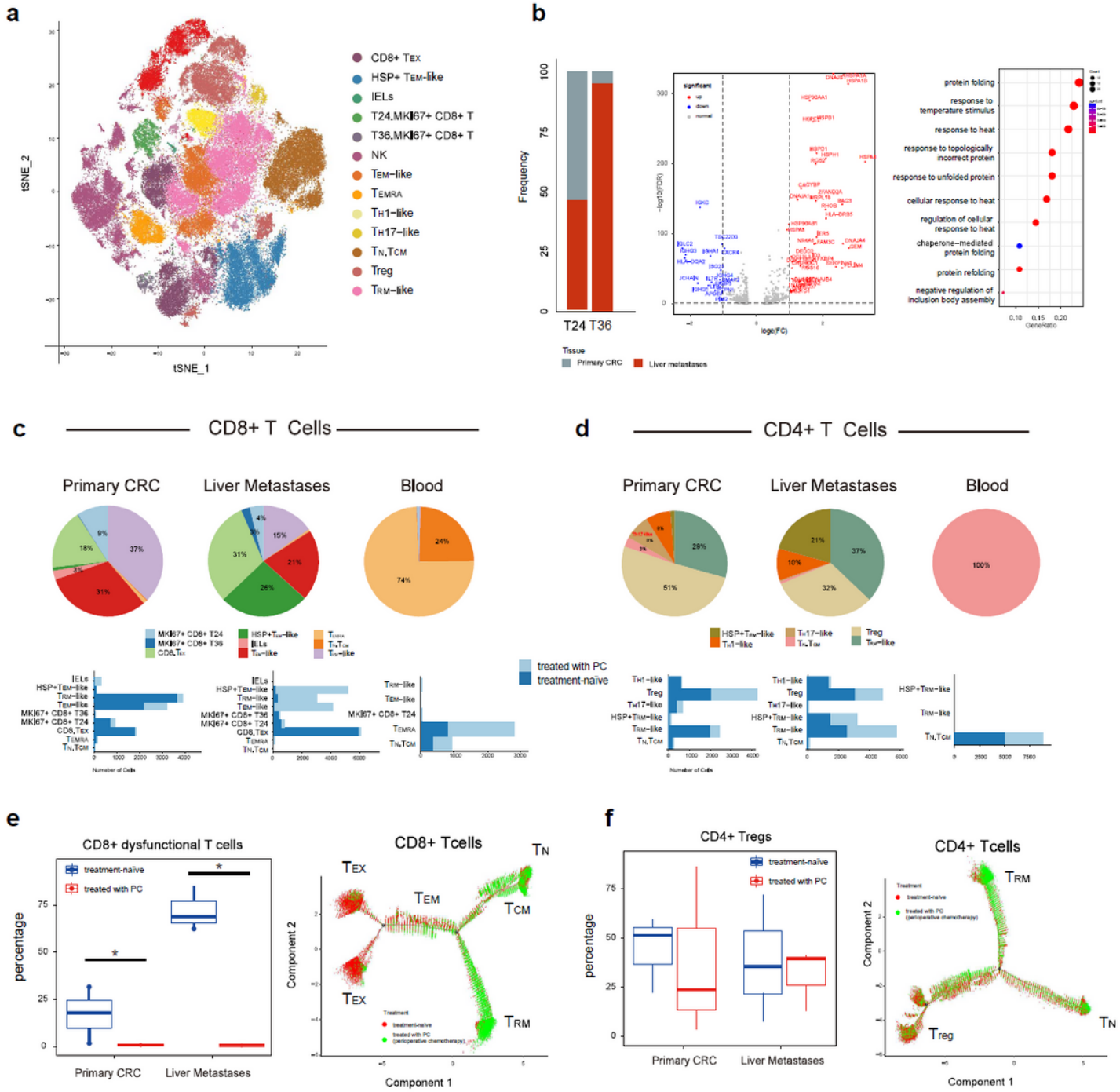

Figure 5

Cell subpopulations in T cell compartments. a, tSNE plot showing a total of 86,803 cell clusters defined within T/ NK cell subtypes. b, Bar plot exhibiting cell tissue distribution of T24 and T36 clusters across different tissues (left). Volcano plot showing differentially expressed genes between the T24 and T36 clusters (middle), each red dot denotes an individual gene with adjusted P value <0.01 (two-sides moderated t-test with limma) and fold change≥2. GO analysis of DEGs (right) between T24 and T36. Selected GO terms with Benjamini-Hochberg-corrected P values <0.05 (one-sided Fisher's exact test) are shown. c, d, Based on the annotation and classification above, the bar plot depicting the number of cells in each cell type of CD8+ T cells (c) and CD4+ T cells (d) for different treatment status for scRNA-seq

profiles. Pie charts showing the proportions of different T cell subsets within different tissues (the primary CRC, liver metastases and blood). e,f, Frequencies of the CD8+ dysfunctional T cells (e) and Treg (f) in each patient in the primary CRC and liver metastases respectively. Wilcoxon rank-sum test was used for statistical analysis. *p < 0.05, **p < 0.01, ***p < 0.001. Developmental trajectory of CD8+ T cells (e) and CD4+ T cells (f) along pseudo-time in two-dimensional space, cells are colored by the treatment state.

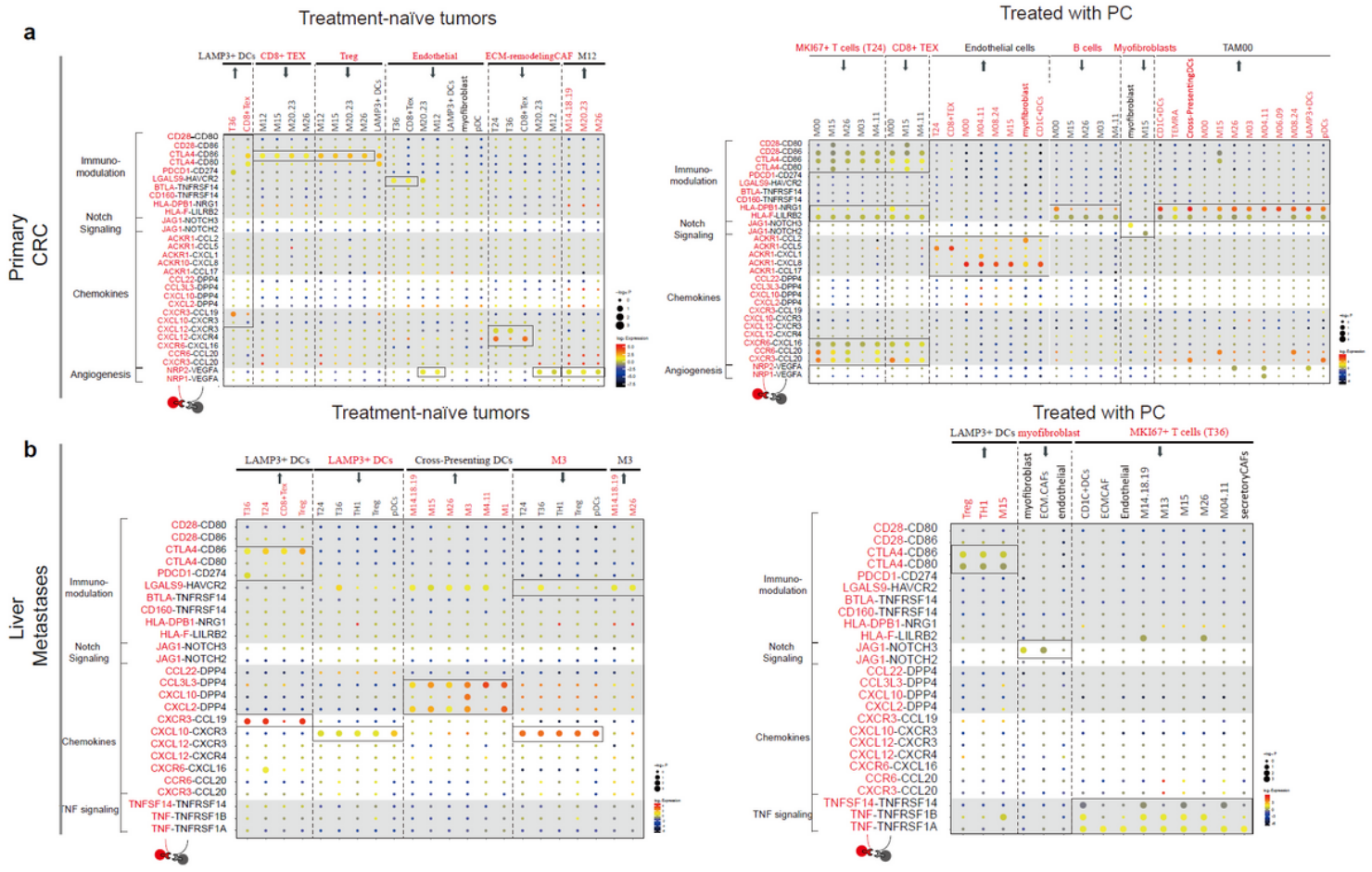

Figure 6

Cell-to-cell signaling networks in liver metastases of CRC. a, Dot plot depicting the selected ligand-receptor interactions enriched in treatment-naïve tumors (left) and tumors treated with preoperative chemotherapy (right) in the primary CRC. Color intensity corresponds to the mean of average expression, dot size indicate the P values, scale on right. b, Dot plot depicting the selected ligand-receptor interactions enriched in treatment-naïve tumors (left) tumors and treated with preoperative chemotherapy (right) in the liver metastases. Molecules colored by red response to they were expressed by cells colored by red. (ECM.CAFs, ECM-remodeling CAFs. Endothelial, endothelial cells).

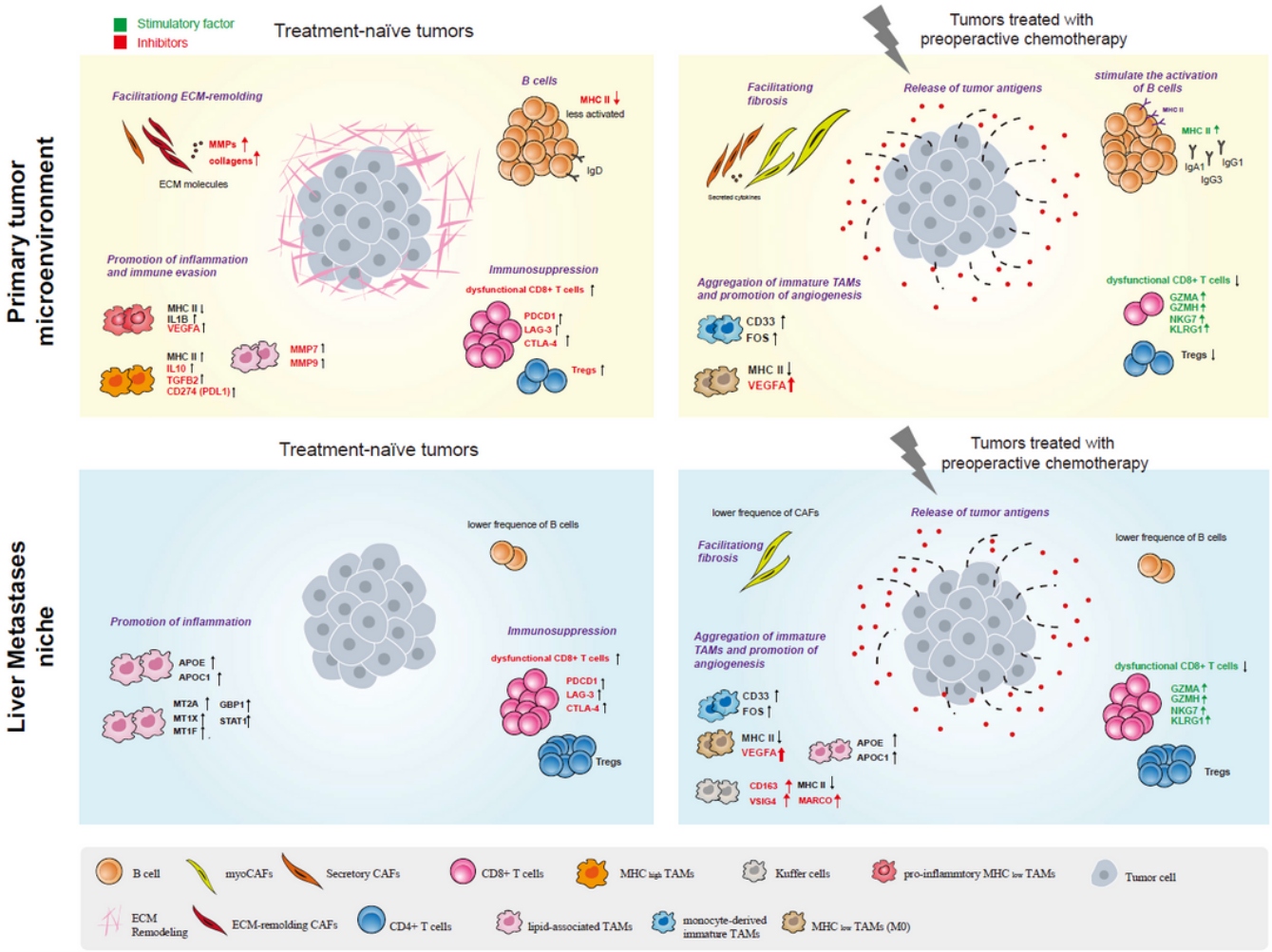

Figure 7

Diagram illustrating the reprogram of TME to response to preoperative chemotherapy.

Supplementary Files

This is a list of supplementary files associated with this preprint. Click to download.

- FigureS1S6.Merge.pdf
- TableS1.xlsx
- FigureS1S6.Merge.pdf
- TableS2.xlsx
- TableS3.xlsx
- TableS4.xlsx
- TableS5.xlsx